

GA-NIFS: Mapping $z \simeq 3.5$ AGN-driven ionized outflows in the COSMOS field

E. Bertola¹, G. Cresci¹, G. Venturi², M. Perna³, C. Circosta^{4,5}, G. Tozzi⁶, I. Lamperti^{7,1}, C. Vignali^{8,9}, S. Arribas³, A. J. Bunker¹⁰, S. Charlot¹¹, S. Carniani², R. Maiolino^{12,13,14}, B. Rodríguez Del Pino³, H. Übler⁶, C. J. Willott¹⁵, T. Böker¹⁶, M. A. Marshall¹⁷, E. Parlanti², J. Scholtz^{12,13}

¹ INAF–OAA, Osservatorio Astrofisico di Arcetri, largo E. Fermi 5, 50127, Firenze, Italy

² Scuola Normale Superiore, Piazza dei Cavalieri 7, I-56126 Pisa, Italy

³ Centro de Astrobiología (CAB), CSIC–INTA, Cra. de Ajalvir Km. 4, 28850 – Torrejón de Ardoz, Madrid, Spain

⁴ Institut de Radioastronomie Millimétrique (IRAM), 300 Rue de la Piscine, 38400 Saint-Martin-d’Hères, France

⁵ European Space Agency, ESAC, Villanueva de la Cañada, E-28692 Madrid, Spain

⁶ Max-Planck-Institut für extraterrestrische Physik (MPE), Gießenbachstraße 1, 85748 Garching, Germany

⁷ Università di Firenze, Dipartimento di Fisica e Astronomia, via G. Sansone 1, 50019 Sesto F.no, Firenze, Italy

⁸ Dipartimento di Fisica e Astronomia “Augusto Righi”, Università degli Studi di Bologna, via P. Gobetti 93/2, 40129 Bologna, Italy

⁹ INAF–OAS, Osservatorio di Astrofisica e Scienza dello Spazio di Bologna, via P. Gobetti 93/3, 40129 Bologna, Italy

¹⁰ Department of Physics, University of Oxford, Denys Wilkinson Building, Keble Road, Oxford OX1 3RH, UK

¹¹ Sorbonne Université, CNRS, UMR 7095, Institut d’Astrophysique de Paris, 98 bis bd Arago, 75014 Paris, France

¹² Kavli Institute for Cosmology, University of Cambridge, Madingley Road, Cambridge, CB3 0HA, UK

¹³ Cavendish Laboratory – Astrophysics Group, University of Cambridge, 19 JJ Thomson Avenue, Cambridge, CB3 0HE, UK

¹⁴ Department of Physics and Astronomy, University College London, Gower Street, London WC1E 6BT, UK

¹⁵ NRC Herzberg, 5071 West Saanich Rd, Victoria, BC V9E 2E7, Canada

¹⁶ European Space Agency, c/o STScI, 3700 San Martin Drive, Baltimore, MD 21218, USA

¹⁷ Los Alamos National Laboratory, Los Alamos, NM 87545, USA

e-mail: elena.bertola@inaf.it

June 12, 2025

ABSTRACT

Active galactic nuclei (AGNi) are a key ingredient in galaxy evolution and possibly shape galaxy growth through the generation of powerful outflows. Little is known regarding AGN-driven ionized outflows in moderate-luminosity AGNi ($\log(L_{\text{bol}}/\text{erg s}^{-1}) < 47$) beyond cosmic noon ($z \gtrsim 3$). In this work we present the first systematic analysis of the ionized outflow properties of a sample of seven X-ray-selected AGNi ($\log(L_X/\text{erg s}^{-1}) > 44$) from the COSMOS-Legacy field at $z \simeq 3.5$ and with $\log(L_{\text{bol}}/\text{erg s}^{-1}) = 45.2 - 46.7$ by using JWST NIRSpec/IFU near-IR spectroscopic observations as part of the “Galaxy Assembly with NIRSpec IFS” (GA-NIFS) program. We spectrally isolated and spatially resolved the ionized outflows by performing a multi-component kinematic decomposition of the rest-frame optical emission lines. JWST/NIRSpec IFU data also revealed a wealth of close-by companions, of both non-AGN and AGN nature, and ionized gas streams likely tracing tidal structures and large-scale ionized gas nebulae extending up to the circumgalactic medium. Ionized outflows were detected in all COS-AGNi targets, with outflow masses in the range $1.5 - 11 \times 10^6 M_\odot$, outflow velocities in the range $\simeq 570 - 3200 \text{ km s}^{-1}$, and mass outflow rates in the range $\simeq 1.4 - 40 M_\odot \text{ yr}^{-1}$. We compared the outflow properties of AGNi presented in this work with previous results from the literature up to $z \simeq 3$, which were opportunely (re-)computed for a coherent comparison. We normalized outflow energetics (\dot{M}_{out} , \dot{E}_{out}) to the outflow density in order to standardize the various assumptions that were made in the literature. Our choice is equal to assuming that each outflow has the same gas density. We find GA-NIFS AGNi to show outflows consistent with literature results, within the large scatter shown by the collected measurements, thus suggesting no strong evolution with redshift in terms of total mass outflow rate, energy budget, and outflow velocity for fixed bolometric luminosity. Moreover, we find no clear redshift evolution of the ratio of mass outflow rate and kinetic power over AGNi bolometric luminosity beyond $z > 1$. In general, our results indicate no significant evolution of the physics driving outflows beyond $z \simeq 3$.

Key words. galaxies: high-redshift – galaxies: active – galaxies: supermassive black holes – ISM: jets and outflows

1. Introduction

A key phase of galaxy evolution is the fast transition ($< 2 \text{ Gyr}$) from early galaxy and black-hole assembly at cosmic dawn (i.e., $z > 6$) to the peak of both the cosmic star formation (SF) rate and the supermassive black hole (SMBH) accretion density at cosmic noon ($z \simeq 1 - 3$; e.g., Madau & Dickinson 2014, and references therein). Despite the present evidence for a key role of

active galactic nuclei (AGNi; (e.g., Magorrian et al. 1998; Strateva et al. 2001; McConnell et al. 2011; Harrison 2017; Caglar et al. 2023)), a comprehensive understanding of AGN-galaxy co-evolution and feedback processes is still far off (e.g., Kormendy & Ho 2013; Harrison et al. 2018; Harrison & Ramos Almeida 2024).

Accretion onto an SMBH is a very powerful process that can release great amounts of energy into the interstellar medium (ISM) of galaxies, giving rise to AGN-driven winds at all scales and in all gas phases (e.g., [Cicone et al. 2018](#); [Costa et al. 2020](#); [Harrison & Ramos Almeida 2024](#); [Ward et al. 2024](#)). Powerful AGN-driven outflows are indeed one of the main channels to establish the AGN-galaxy coevolution (e.g., [King & Pounds 2015](#); [Costa et al. 2018](#)). Especially in the past fifteen years, great effort has been expended by the community to characterize AGN-driven winds and their impact on AGNi host galaxies (e.g., see [Cresci & Maiolino 2018](#); [Veilleux et al. 2020](#); [Laha et al. 2021](#); [Harrison & Ramos Almeida 2024](#), for recent reviews). Such winds originate from the inner regions of galaxies and are observable in X-rays (e.g., [Cappi et al. 2006](#); [Igo et al. 2020](#); [Charatas et al. 2021](#); [Matzeu et al. 2023](#)), and they expand up to galactic scales as neutral (e.g., [Morganti et al. 2016](#)), ionized (e.g., [Harrison et al. 2012](#); [Genzel et al. 2014](#); [Carniani et al. 2015, 2017](#); [Förster Schreiber et al. 2019](#); [Kakkad et al. 2020](#); [Cresci et al. 2023](#); [Tozzi et al. 2024](#)), and molecular outflows (e.g., [Ferguson et al. 2017](#); [Brusa et al. 2018](#)), which are traced in the optical and submillimeter rest-frame bands (e.g., [Cicone et al. 2018](#)). Studies in the local Universe (e.g., [Fluetsch et al. 2019](#)) up to cosmic dawn (e.g., [Bischetti et al. 2022](#)) have demonstrated the ubiquitous presence of such AGN-driven winds, which often carry a kinetic power that could indeed affect the SF of their hosts ($\dot{E}_{\text{out}}/L_{\text{bol}} > 0.5 - 5\%$, [Di Matteo et al. 2005](#); [Hopkins & Elvis 2010](#)).

The ionized outflow component has been traced mainly through the [O III] and H α optical emission lines (e.g., [Cano-Díaz et al. 2012](#); [Perna et al. 2015a](#); [Harrison et al. 2016](#); [Leung et al. 2019](#)), probing gas motions up to kiloparsec scales from the AGN. On the one hand, tracing outflows with the H α emission line offers the advantage of converting the line luminosity into ionized gas mass without assumptions regarding the gas metallicity ([Cresci et al. 2015a](#); [Carniani et al. 2015](#)), but it risks possible contamination of emission from the broad-line region (BLR) in Type 1 AGNi. On the other hand, the [O III] doublet is a forbidden line transition that can only originate in low-density regions. Thus in principle, it is free of contamination by emission from a higher-density region, such as that of the BLR, yet the gas metallicity has to be known (or assumed) in order to convert its luminosity into ionized gas mass. Moreover, H α emission is often less affected by outflows and therefore can be used to better identify rotating motions in the ISM (e.g., [Perna et al. 2022](#)) as well as gas ionized by star-forming regions in the AGN host. The latter is particularly important to unveiling possible anticorrelations between outflowing gas and SF gas and thus to testing feedback scenarios (e.g., [Cresci et al. 2015b](#); [Cresci & Maiolino 2018](#), but see also [Scholtz et al. 2020](#)). While spatially integrated spectra can efficiently probe ionized outflows beyond the local Universe (e.g., [Perna et al. 2015b](#); [Leung et al. 2019](#); [Temple et al. 2024](#)), only integral field spectroscopy (IFS) allows unperturbed motions (e.g., rotation) to be disentangled from galaxy-wide outflows (e.g., [Venturi et al. 2018](#); [Gallagher et al. 2019](#); [Zanchettin et al. 2023](#); [Travascio et al. 2024](#); [Ulivi et al. 2024](#); [Speranza et al. 2024](#)). However, ground-based near-infrared (NIR) integral field units (IFUs) can observe the rest-frame ionized emission only up to $z \approx 2.6$ in the H α line and up to $z \approx 3.5$ in the [O III] line, while for higher redshift, these lines are redshifted out of the K band (e.g., [Cano-Díaz et al. 2012](#); [Harrison et al. 2012](#); [Carniani et al. 2015, 2016](#); [Davies et al. 2020b](#); [Kakkad et al. 2020](#); [Vayner et al. 2021b,a](#); [Tozzi et al. 2024](#)).

Powerful AGNi are expected to drive the most prominent outflows (e.g., [Cicone et al. 2014](#); [Fiore et al. 2017](#); [Fluetsch et al. 2019](#); [Musiimenta et al. 2023](#)). They are also the least challenging systems to observe beyond the local Universe and have allowed in-depth analyses up to $z \gtrsim 3$ (e.g., [Bischetti et al. 2017](#); [Perrotta et al. 2019](#)). However, it is critical to investigate AGN feedback also in galaxies hosting AGN of less extreme power ($\log(L_{\text{bol}}/\text{erg s}^{-1}) < 47$) since they are the majority of the AGNi population. This was well addressed at cosmic noon by the KASHz (KMOS AGN Survey at High redshift, PI: D. Alexander; [Harrison et al. 2016](#), Scholtz et al., in prep.) and the SUPER¹ (SINFONI Survey for Unveiling the Physics and Effect of Radiative feedback, PI: V. Mainieri; [Circosta et al. 2018](#)) surveys. Investigating AGN-driven outflows and feedback effects in sources that were selected solely based on their X-ray luminosity, both surveys showed that powerful AGN-driven ionized outflows are common at cosmic noon ([Harrison et al. 2016](#); [Kakkad et al. 2020](#); [Tozzi et al. 2024](#), see also [Vietri et al. 2020](#) for UV-traced winds), but the surveys were limited to $z \lesssim 2.6$ by the goal of also mapping the unobscured SF in the H α line.

Until recently, outflows in the $z \approx 3 - 7$ redshift range could only be probed through spatially integrated rest-frame UV data (e.g., [Yang et al. 2021](#); [Vietri et al. 2022](#)) and in the submillimeter bands ([Bischetti et al. 2019a](#); [Puglisi et al. 2021](#)). The James Webb Space Telescope (JWST; [Gardner et al. 2023](#)) now provides the first optical rest-frame view of AGNi in this redshift range and the additional benefit of IFS at sub-kiloparsec resolution using the NIRSpec IFU mode ([Böker et al. 2022](#); [Jakobsen et al. 2022](#)). The capabilities of JWST range from observing the ionized gas component in host galaxies of high-redshift quasars up to $z > 7$ (e.g., [Harikane et al. 2023](#); [Cresci et al. 2023](#); [Loiacono et al. 2024](#); [Liu et al. 2024](#)) to resolving the rich environment in the immediate neighborhood of AGNi, in which case it often shows companions and merger features (e.g., [Perna et al. 2025b, 2023](#); [Marshall et al. 2024](#)).

In this work, we present the analysis of a sample of AGNi selected from the X-ray COSMOS-Legacy deep field ([Marchesi et al. 2016](#)) and targeted by the JWST Near Infrared Spectrograph (NIRSpec) within the Guaranteed Time Observations (GTO) program “Galaxy Assembly with NIRSpec IFS” (GA-NIFS²; PI: R. Maiolino and S. Arribas). We present our sample in Sect. 2, the data reduction in Sect. 3, and the data analysis in Sect. 4. We discuss our results in Sect. 5, where we present the properties of each source and the derivation of outflow properties. In Sect. 6, we compare the outflows of COS-AGNi with results present in the literature, and we summarize our results in Sect. 7. Throughout this work, we adopt a [Chabrier \(2003\)](#) initial mass function ($0.1 - 100 M_{\odot}$) and a flat Λ CDM cosmology ([Planck Collaboration et al. 2020](#)), with $H_0 = 67.7 \text{ km s}^{-1} \text{ Mpc}^{-1}$ and $\Omega_{\text{m},0} = 0.31$ throughout the paper. For all the maps shown in this work, north is up and east is to the left.

2. COS-AGNi in GA-NIFS: an uncharted L_{bol} range at $z > 3$

The GA-NIFS program targeted 55 objects (AGNi and galaxies) at $z \sim 2 - 11$ with NIRSpec IFU during JWST cycles 1 and 3, totaling more than 300 hr of exposure time. In this work we focus on the AGNi selected from COSMOS-Legacy, which consist of six X-ray-selected systems at $z \approx 3.5$ (see [Perna et al.](#)

¹ <http://www.super-survey.org/>

² <https://ga-nifs.github.io>

Table 1: Summary of AGN and host galaxy properties of the COS-AGNi GA-NIFS sample.

Target	RA (deg)	DEC (deg)	z_{spec}	Type	$\log N_{\text{H}}$ (cm^{-2})	$\log L_{2-10\text{keV}}$ (erg s^{-1})	$\log L_{\text{bol}}$ (erg s^{-1})	$\log M_{\star}$ (M_{\odot})	SFR ($M_{\odot} \text{ yr}^{-1}$)	$A_{\text{v}}^{\text{tot}}$ (mag)	$A_{\text{v}}^{\text{nar}}$ (mag)
(1)	(2)	(3)	(4)	(5)	(6)	(7)	(8)	(9)	(10)	(11)	(12)
COS590	149.755412	+2.73853	3.52385 ± 0.00002	1	< 23.2	44.41	45.57 ± 0.14	10.7 ± 0.07	< 11	0.6 ± 0.1	1.3 ± 0.1
COS1118	149.879192	+2.22584	3.64300 ± 0.00003	1	< 20	44.30	45.2 ± 0.15	10.48 ± 0.17	< 43	1.1 ± 0.1	0.9 ± 0.1
COS349	150.004377	+2.03892	3.5093 ± 0.0003	1	< 20	44.26	46.17 ± 0.02	< 10.56	< 116	0.9 ± 0.1^a	—
COS1656-A	150.271546	+1.61383	3.5101 ± 0.0004	2	—	44.43^{\ddagger}	< 45.84	10.95 ± 0.04	< 80	2.2 ± 0.9	—
COS2949	150.402917	+1.87889	2.0478 ± 0.0003	2	$23.65^{+0.28}_{-0.23}^*$	$44.48^{+0.24}_{-0.26}^*$	45.36 ± 0.11	10.44 ± 0.1	57 ± 2	3.2 ± 0.1^b	—
COS1638*	—	—	—	—	$< 23.5^{\ddagger}$	44.50^{\ddagger}	46.78 ± 0.02	11.08 ± 0.19	1947 ± 58	—	—
COS1638-A	150.735557	+2.19953	3.5057 ± 0.0001	1	—	—	$46.7 \pm 0.3^{\ddagger}$	—	—	0.9 ± 0.1^a	1.2 ± 0.1
COS1638-B	150.735847	+2.19962	3.5109 ± 0.0001	2	—	—	$46.2 \pm 0.3^{\ddagger}$	—	—	4.2 ± 0.8	—

Notes. (1) Target ID; (2)-(3) Coordinates; (4) Spectroscopic redshift determined from the narrow component of the [O III] line; (5) AGN Type; (6)-(7) Column density and X-ray luminosity from Marchesi et al. (2016); (8)-(10) SED fitting results (AGN bolometric luminosity, stellar mass, star formation rate; Circosta et al., in prep.); (11)-(12) Dust extinction for total emission and narrow components, respectively. *: The parameters of COS1638 refer to X-ray data and SED fitting performed on photometry that are spatially integrated over AGNi A and B of this dual system. †: Bolometric luminosity as measured in Perna et al. (2025b). ‡: Dual AGN that is not spatially resolved in COSMOS-Legacy, X-ray parameters are referred to the integrated system. *: X-ray properties estimated from dedicated fitting of the X-ray spectrum using the spectroscopic redshift measured in this work. ^a: Dust extinction measured as the median of the other Type 1 COS-AGNi (COS1118, COS590). ^b: Dust extinction measured as the median of the other Type 2 COS-AGNi (COS1638-B, COS1656-A).

2025b). Such a narrow redshift range was specifically selected to simultaneously observe all the primary optical emission lines, from [O II] $\lambda 3726, 3728$ to [S II] $\lambda \lambda 6717, 6730$, within one single NIRSpec grating (G235H/F170LP). Two of the observed systems are dual AGNi (COS1656 and COS1638), thus increasing the sample size to eight AGNi. We exclude the secondary AGN of the COS1656 system (COS1656-B) because of its complex line profiles, which could be due to tidal interactions, outflows or simply the superposition with another system along the line of sight (Perna et al. 2025b). Moreover, one AGN (COS2949) was wrongly identified as a $z \approx 3.5$ object in the COSMOS-Legacy catalog, and JWST/NIRSpec data unambiguously uncovered a $z \approx 2$ AGN spectrum (see Sect. 5.2). Despite its lower redshift ($z \approx 2$), we do not exclude COS2949 from our sample, and we highlight it in the plots to differentiate it from the other COS-AGNi at $z \approx 3.5$. The sample of COSMOS AGNi used in this work (COS-AGNi sample henceforth) comprises only X-ray-selected AGN (and their secondary, if dual), totaling seven AGN with median redshift $z \approx 3.5$: four Type 1s (COS1118, COS590, COS1638-A, COS349) and three Type 2s (COS1656-A, COS1638-B, COS2949). AGN classification in Type 1/Type 2 based on the presence/absence of AGN broad lines in the rest-frame UV/optical data is part of the COSMOS-Legacy catalog of Marchesi et al. (2016) and JWST data have confirmed it. AGN and host galaxy properties were retrieved through dedicated SED fitting with CIGALE (Boquien et al. 2019; Yang et al. 2020, 2022), using photometry from the rest-frame UV-optical to FIR, including that available from JWST imaging in the COSMOS field. Photometry collection and SED fitting of the full GA-NIFS AGNi sample will be presented in a forthcoming paper (Circosta et al., in prep.), including the derivation of host galaxy properties and AGN bolometric luminosities, which are found to range between $L_{\text{bol}} = 10^{45} - 10^{47} \text{ erg s}^{-1}$. Table 1 summarizes the properties of COS-AGNi presented in this work and Figure 1 (right) shows the $\text{SFR}-M_{\star}$ distribution of GA-NIFS AGNi, including those selected from GOODS-S (Übler et al. 2023; Parlanti et al. 2024; Perna et al. 2025a; Venturi et al., in prep.).

Figure 1 (left) shows the $L_{\text{bol}}-z$ distribution of GA-NIFS AGNi. Building on the compilation in Circosta et al. (2018) and Scholtz et al. (2023), we also show in the $L_{\text{bol}}-z$ panel AGNi from the literature that were studied for their AGN-driven ionized outflows. We show both targets investigated with spatially integrated spectra (green markers; Shen 2016; Bischetti et al.

2017; Vietri et al. 2018; Coatman et al. 2019; Perrotta et al. 2019; Leung et al. 2019; Temple et al. 2019, 2024; Musiimenta et al. 2023) and IFU data (blue markers; Vietri et al. 2018; Davies et al. 2020b; Kakkad et al. 2020; Vayner et al. 2021b,a; Tozzi et al. 2021, 2024; Lau et al. 2024)³. The compilation by Fiore et al. (2017)⁴ includes both spatially integrated and IFU spectra of AGNi from the local Universe up to $z \lesssim 3.4$. We further expand the $z < 1$ compilation (black markers) with the following works, not included in Fiore et al. (2017): Liu et al. (2014); Husemann et al. (2013, 2014, 2017); Harrison et al. (2014); Karouzos et al. (2016); Rupke et al. (2017); Perna et al. (2017); Baron & Netzer (2019); Bessiere et al. (2024). For the sources presented in Bessiere et al. that were already included in the compilation of Fiore et al. (2017), we consider the more recent analysis of Bessiere et al. (2024). We also show AGNi recently targeted by JWST/NIRSpec IFU (Cresci et al. 2023; Suh et al. 2025; Vayner et al. 2024; Loiacono et al. 2024), including results from the GA-NIFS program (Marshall et al. 2023; Übler et al. 2023; Perna et al. 2023; Parlanti et al. 2024; Zamora et al. 2024; Perna et al. 2025a). Moreover, we include the AGNi newly discovered by JWST through spatially integrated NIRSpec spectra (Scholtz et al. 2023; Maiolino et al. 2024; Harikane et al. 2023; Kocevski et al. 2023; Carnall et al. 2023; Greene et al. 2024; Furtak et al. 2024; Chisholm et al. 2024) up to $z \approx 7$ for showing purposes. Figure 1 highlights the capabilities of JWST/NIRSpec IFU and the novelty of the GA-NIFS sample: we are probing for the first time the ionized gas properties of galaxies harboring AGNi of $45.2 < \log(L_{\text{bol}}/\text{erg s}^{-1}) < 46.7$ at $z > 2.6$, a L_{bol} range that is well studied only at lower redshifts. Moreover, GA-NIFS AGNi are the first sample of AGNi at $z > 3$ for which spatially resolved rest-frame optical spectroscopy is available. We note that this $z-L_{\text{bol}}$ range is partly probed by Keck/MOSFIRE (spatially integrated) spectra that only cover the $H\beta + [\text{O III}]$ complex

³ We refer to Saccheo et al. (2023) for the bolometric luminosities of AGNi selected from the WISE/SDSS selected Hyper-luminous quasars sample (WISSH; Bischetti et al. 2017; Vietri et al. 2018).

⁴ The compilation of Fiore et al. (2017) includes results from the following studies: Nesvadba et al. (2006, 2008); Alexander et al. (2010); Cano-Díaz et al. (2012); Harrison et al. (2012); Maiolino et al. (2012); Harrison et al. (2014); Rupke & Veilleux (2013); Liu et al. (2013a,b); Genzel et al. (2014); Brusa et al. (2015); Cresci et al. (2015a); Carniani et al. (2015); Perna et al. (2015a,b); Cicone et al. (2015); Zakamska et al. (2016); Brusa et al. (2016); Wylezalek et al. (2016); Bischetti et al. (2017); Duras et al. (2017).

($\log(L_{\text{bol}}/\text{ergs}^{-1}) > 45.7$, Trakhtenbrot et al. 2016), the low S/N and lower spectral resolution of which hampered the investigation of outflows.

3. Observations and data reduction

COS-AGNi were observed for 3560s of on-source time each between April and May 2023 (PID: 1217, PI: Nora Lützgendorf) with NIRSpec IFU in the G235H/F170LP grating/filter configuration (resolving power $R \approx 2700$). These observations were tailored at spatially and spectrally isolating fast AGN-driven outflows from the systemic emission of the host galaxy. They cover rest-frame optical nebular emission lines (e.g., [O II] $\lambda 3726, 3728$, H β , [O III] $\lambda 4959, 5007$, H α , [N II] $\lambda 6548, 6583$ and [S II] $\lambda \lambda 6717, 6730$) providing the unprecedented spatial resolution of 350pc/spaxel at $z \approx 4$ in the NIR (for a 0.05'' spaxel size). We present the three-color images of COS-AGNi in Figure 2.

Raw data files were downloaded from the MAST archive and subsequently processed with the JWST Science Calibration pipeline version 1.8.2 under CRDS context `jwst_1068.pmap`. We made several modifications to the default three-stages reduction to increase data quality, which are described in detail by Perna et al. (2023) and briefly reported here. We patched the pipeline to avoid oversubtraction of the elongated cosmic ray artifacts during Stage1. The individual count-rate frames were further processed at the end of the Stage1 pipeline, to correct for different zero-level in the individual (dither) frames, and subtract the vertical 1/f noise. In addition, we made the following corrections to the `*cal.fits` files after Stage 2: we masked pixels at the edge of the slices (two pixels wide) to conservatively exclude those with unreliable `sflat` corrections; we removed regions affected by leakage from failed open shutters; finally, we used a modified version of LACOSMIC (van Dokkum 2001) to reject strong outliers before the construction of the final data cube (D'Eugenio et al. 2024). The final cubes were combined using the drizzle method with pixel scales of 0.05'', for which we used an official patch to correct a known bug, as implemented in the pipeline v1.9.0 and higher.

The spatial under-sampling of the point spread function (PSF) of NIRSpec produces the so-called “wiggles” in the single-spaxel spectra of bright targets. Such an effect is mitigated when extracting 1-D spectra over larger apertures, as a reference, typically larger than 0.2''–0.5''. Perna et al. (2023) developed an algorithm⁵ to correct for this effect since there is no available correction in the data reduction pipeline. We therefore applied this algorithm to correct for the wiggles in our cubes. We briefly summarize it here and refer the interested reader to Perna et al. (2023) for additional details. We model the wiggles as a sinusoidal function in the spectrum extracted from the brightest spaxel of the cube. Wiggle modeling is performed after masking the narrow emission lines, the broad line profiles (e.g., we mask the full H α complex) and the NIRSpec spectral gap between the two detectors. Masking the lines is a necessary step to avoid mistaking the broad line wings for an under-sampling-induced modulation of the signal. The wiggles model is built in an iterative approach over small portions of the wavelength range, until the corrected single-spaxel spectrum of the brightest spaxel fairly resembles the integrated spectrum from a larger aperture, in which the effects of wiggles disappear. For our targets, we extract the integrated 1-D spectrum from an aperture centered at the H α

emission peak and of 5-pixel radius (0.25''), which we find to be large enough for the wiggles effect to disappear in our data.

The cubes of COS1638 and COS1656 show the most prominent wiggles, likely because they are the brightest targets in the sample. COS1118, COS590 and COS349 present much less prominent wiggles, yet they would still hamper a correct spaxel-by-spaxel fitting and as such we correct their cubes for this effect. We do not observe wiggles in the NIRSpec cube of COS2949 and thus such a correction is deemed unnecessary.

4. Data analysis

We present in this section the analysis of the NIRSpec IFU data, which was carried out both in a spaxel-by-spaxel approach (Sect. 4.1) and on 1-D spectra (Sect. 4.2) integrated over entire spatial extension of the outflows to best determine their properties. Spectroscopic redshifts are estimated from the peak of the [O III] narrow emission component in the integrated spectra.

4.1. Spaxel-by-spaxel spectral fitting

We follow the procedure outlined in Marasco et al. (2020) and Tozzi et al. (2021) to derive the kinematic properties of ionized gas in the NLR, star-forming regions, and any kpc-scale structure surrounding the host galaxies (e.g., tidal tails and companions) of COS-AGNi, as traced by the main rest-frame optical emission lines like H β , [O III] $\lambda 4759, 5007$, H α , [N II] $\lambda 6548, 6583$ and [S II] $\lambda \lambda 6717, 6730$. This fitting procedure aims at producing cubes of the ionized-gas component by modeling and subtracting any (stellar and/or AGN) continuum and unresolved AGN BLR emission, if present. Hereafter, we will refer to the cubes produced after continuum and AGN BLR subtraction as the ionized-gas cubes.

As described in Tozzi et al. (2021), this fitting approach is comprised of three main steps for Type 1 AGNi: *i*) first, we extract a high signal-to-noise ratio (S/N) spectrum from the nuclear region of the AGN to fit the broad lines and produce a BLR template; *ii*) we fit the full data cube spaxel-by-spaxel, including a polynomial or power-law function to reproduce the continuum and letting the BLR template vary only in amplitude, and subtract the BLR+continuum best-fit; *iii*) we fit the BLR+continuum-subtracted cube with a spaxel-by-spaxel approach to derive the gas kinematical properties at galaxy scales. For Type 2 AGNi, the fitting procedure comprises only step *ii*) and *iii*) given the absence of emission from the BLR. Both for Type 1 and Type 2 AGNi, we use the nuclear spectrum to measure the source redshift (as listed in Table 1) from the narrow peak of the [O III] $\lambda 5007$ line in a multi-Gaussian fit (with one to three components based on the least number of components returned by the Kolmogorov-Smirnov test in step *iii*)). We use the [O III] $\lambda 5007$ line for all targets but COS2949, whose redshift was anchored to the H α narrow peak since the [O III] falls blueward of the NIRSpec's wavelength range, and for COS1638-A, for which we use the narrow H α peak since the [O III] line is dominated by the outflows also in the nuclear spectrum.

4.1.1. Modeling of BLR lines and continuum template

In step *i*), we model the BLR emission lines using a nuclear-emission spectrum integrated from a circular region of radius 1 spaxel (0.05'') centered on the spaxel with the highest H α flux. We use a broken power-law model convolved with a Gaussian core to best reproduce the broad emission line profiles and their

⁵ The algorithm by Perna et al. (2023) is available at https://github.com/micheleperna/JWST-NIRSpec_wiggles.

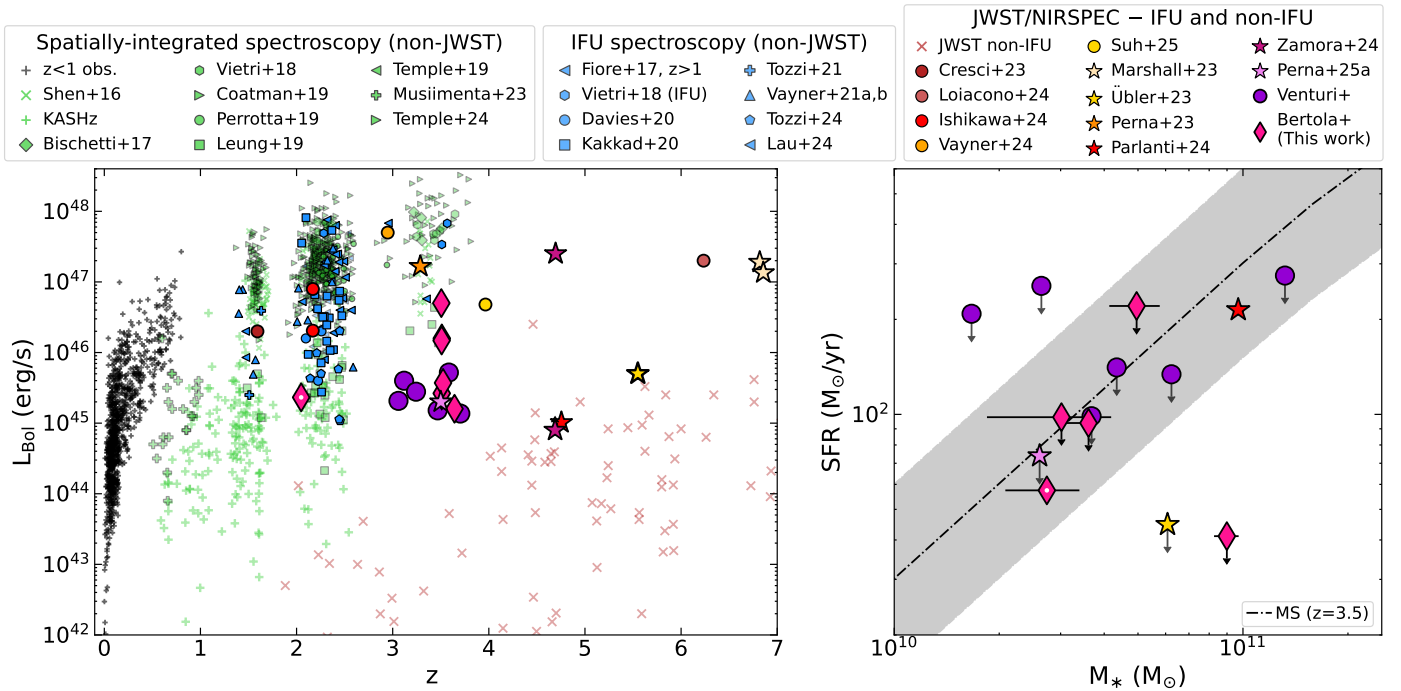


Fig. 1: General properties of GA-NIFS AGN and summary of IFS observations from the literature. *Left*: Bolometric luminosity versus redshift distribution of the COS-AGN presented in this work (magenta diamonds). Building on the compilations of [Fiore et al. \(2017\)](#) and [Circosta et al. \(2018\)](#) (see their Fig. 1), we also show literature AGN for which optical rest-frame spectroscopy is available and has allowed ionized outflows to be probed, to highlight the new bolometric luminosity range probed by GA-NIFS AGN at $z > 3$. Literature targets are color-coded as follows: a (non-exhaustive) compilation of AGN at $z < 1$ is shown as black crosses (see Sect. 2); AGN studied through spatially integrated spectra are shown as green symbols (see legend and Sect. 2 for details); AGN studied through IFS data are shown as blue symbols (see legend and Sect. 2 for details). Stars and circles mark JWST/NIRSpec IFU observations from GA-NIFS and other surveys, respectively (see legend and Sect. 2 for details). GOODS-S AGN from GA-NIFS that will be presented in Venturi et al. in prep are shown as purple circles. Red x signs show a compilation of AGN and AGN candidates newly discovered by JWST through spatially integrated NIRSpec spectra ([Scholtz et al. 2023](#); [Maiolino et al. 2024](#); [Harikane et al. 2023](#); [Kocevski et al. 2023](#); [Carnall et al. 2023](#); [Greene et al. 2024](#); [Furtak et al. 2024](#); [Chisholm et al. 2024](#)). *Right*: Star formation rate versus stellar mass plot of GA-NIFS AGN to show their relation with the main sequence of star forming galaxies. Both quantities are measured from SED fitting. Color coding is the same as the left panel. A white dot marks COS2949, the COS-AGN at $z \approx 2.05$. The black dash-dotted line is the main sequence of [Schreiber et al. \(2015\)](#) at $z = 3.5$, with the shaded area showing the 0.3 dex scatter.

wings ($H\alpha$, $H\beta$, $H\gamma$, $H\delta$, $\text{HeI}\lambda 5876$, $\text{HeII}\lambda 4687$, when present). We anchor the line shape to the highest S/N broad line in our data, which for all our Type 1 AGN is the $H\alpha$ line. We find the broken power-law best fit from $H\alpha$, and then fit the rest of the broad lines by scaling its peak to match the intensity of each of them (e.g., [Cresci et al. 2023](#)). We model the broad Fe II emission using templates produced with the semi-analytic model released by [Kovačević et al. \(2010\)](#), following the approach of [Marasco et al. \(2020\)](#) and [Tozzi et al. \(2021\)](#). To best model the shape of the broad lines, we included also the NLR contribution as two or three Gaussian components, linked across all the emission lines included in the model, to fully reproduce the line profiles and best disentangle the contribution of BLR and NLR. Throughout our fitting process, we set the flux ratios of $[\text{O III}] \lambda 5007/\lambda 4959$ ($[\text{O III}]$ henceforth), $[\text{N II}] \lambda 6583/\lambda 6548$ ($[\text{N II}]$ henceforth) and $[\text{O I}] \lambda 6300/\lambda 6364$ to the theoretical expectation of 3⁶. The AGN continuum was modeled either as a polynomial of 2nd or 3rd order or as a power law, depending on the continuum shape of the specific target. The resulting BLR template only includes the best fit of the broad Balmer lines and the

Fe II templates. Figures A.1–A.2 show the best-fit of the nuclear spectra of the Type 1 AGN used to produce the BLR template, including continuum and BLR emission.

4.1.2. Modeling of the total emission

In step *ii*), we map the AGN and galaxy emission by fitting the full data cube spaxel-by-spaxel with the Penalized PiXel-Fitting (pPXF) method ([Cappellari & Emsellem 2004](#); [Cappellari 2023](#)). The aim of this step is to model the total continuum emission and, when present, the BLR contribution using the BLR template produced in step *i*) to then subtract them and produce the ionized-gas cube. The BLR emission is produced in the innermost regions of the AGN, and thus it is unresolved in our data. As such, we allowed for the BLR template to scale in intensity throughout the field of view without modification to the shape of its emission lines. The continuum is fit with a polynomial of second or third order, plus the power law continuum of the AGN accretion disk if indicated as best BLR model in step *i*). As in step *i*), we included additional Gaussian components, with velocity shift and broadening linked between all the considered emission lines, to best reproduce the complex line

⁶ <https://www.nist.gov/pml/nist-atomic-spectra-bibliographic-databases>

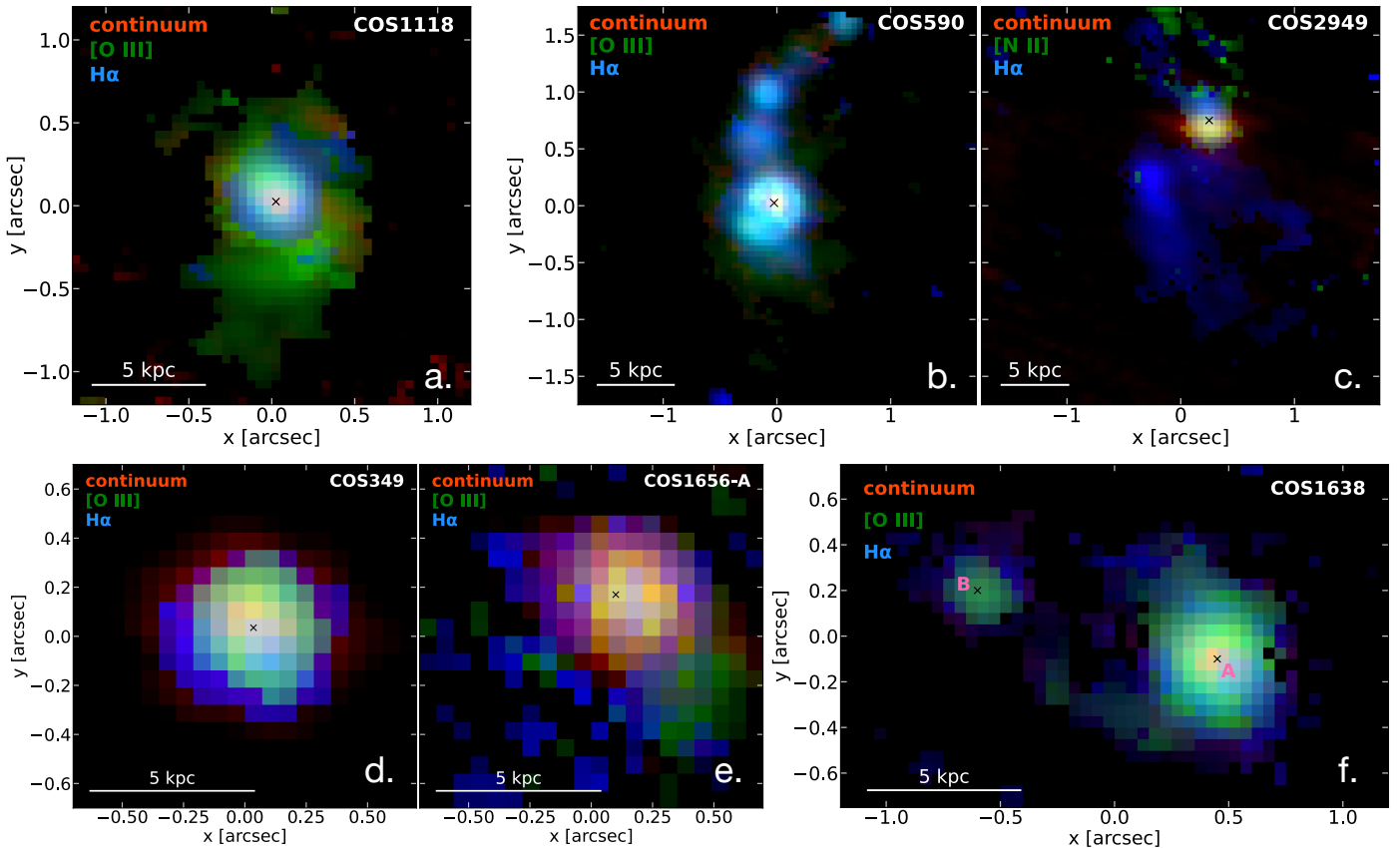


Fig. 2: Three-color images of COS-AGNi from GA-NIFS: Panel a. COS1118; Panel b. COS590; Panel c. COS1949; Panel d. COS349; Panel e. COS1656-A; and Panel f. COS1638-A (right) and -B (left). Red is the continuum, green is total [O III] emission, and blue is total H α emission. For COS2949, green is total [N II] emission, to highlight the position of the AGN. Black crosses mark the position of the AGN. The continuum of COS1118, COS1656-A and COS2949 is measured over the full range probed by NIRSpec ($\approx 3500 - 7000\text{\AA}$ for the first two, $6500 - 10000\text{\AA}$ for the latter), after masking the emission lines. The continuum of COS1638-A and COS349 is measured in the $\approx 5500 - 6300\text{\AA}$ range because lower wavelengths are affected by strong Fe II emission. The continuum of COS590 is measured in the $\approx 3500 - 5200\text{\AA}$ range to exclude the noisier channels of the cube. For this target, we also subtract the field noise in the continuum map as the median of the signal for each pixel column.

profiles arising from the ionized gas and thus model the underlying continuum at best. We ran step *ii* three times, including from one to three Gaussian components, and saved the best fit of each spaxel for each run. Following the Kolmogorov-Smirnov test as implemented by Marasco et al. (2020), we then selected the best model of each spaxel by comparing the residuals of the [O III] and H α lines, i.e. those of interest for our study, modeled with one to three Gaussians in step *ii*.

With this procedure, we obtained the best-fitting model of each spaxel in the full field of view. We then used the models to subtract, spaxel-by-spaxel, the continuum and, when present, the BLR contribution in order to produce the ionized-gas data cubes.

4.1.3. Modeling of the ionized-gas cubes

To increase the S/N in the ionized-gas cubes, we smooth the signal of each cube plane with a Gaussian kernel of size smaller than the instrumental PSF: $\sigma_{\text{smooth}} = 0.05''$ compared to a $FWHM_{\text{PSF}} = 0.1'' - 0.17''$ (D'Eugenio et al. 2024). Despite the careful data reduction, the cube of COS1656 still shows some spurious signal, possibly due to contamination from open MSA shutters. We thus do not smooth the cube of COS1656 to avoid the contaminating signal affecting more spatial pixels. In step

iii, we fit the ionized-gas data cubes spaxel-by-spaxel. As done in step *ii*, we use from one to three Gaussian components linking velocity shift and broadening across the lines with the aim of best reproducing the full line profiles. At this stage, we focus on best modeling our data and do not associate a physical meaning to each component yet. This approach allowed us to correctly reproduce the ionized gas emission of all the analyzed cubes, except for COS1638. In fact, the asymmetries of the [O III] and H α line profiles are not similar enough to be fit together, in the sense that the best fit produced from the [O III] line does not fully reproduce the bluest side of the broad component of H α , and viceversa, for both COS1638-A and COS1638-B. Such different asymmetries may well be caused by an imperfect wiggles correction. For this reason, we fit this cube including two sets of one to three Gaussian components with velocity shift and broadening tied among different lines: one set is tied between H β and [O III], while a second set, with the same number of Gaussian components as the first one, is tied between H α , [N II] and [S II].

As in step *ii*, we then compare the residuals of each model in each spaxel and, applying the Kolmogorov-Smirnov test, we select the minimum number of gas components required to best reproduce the ionized gas emission in each spaxel separately. Three components are typically needed in our data to reproduce

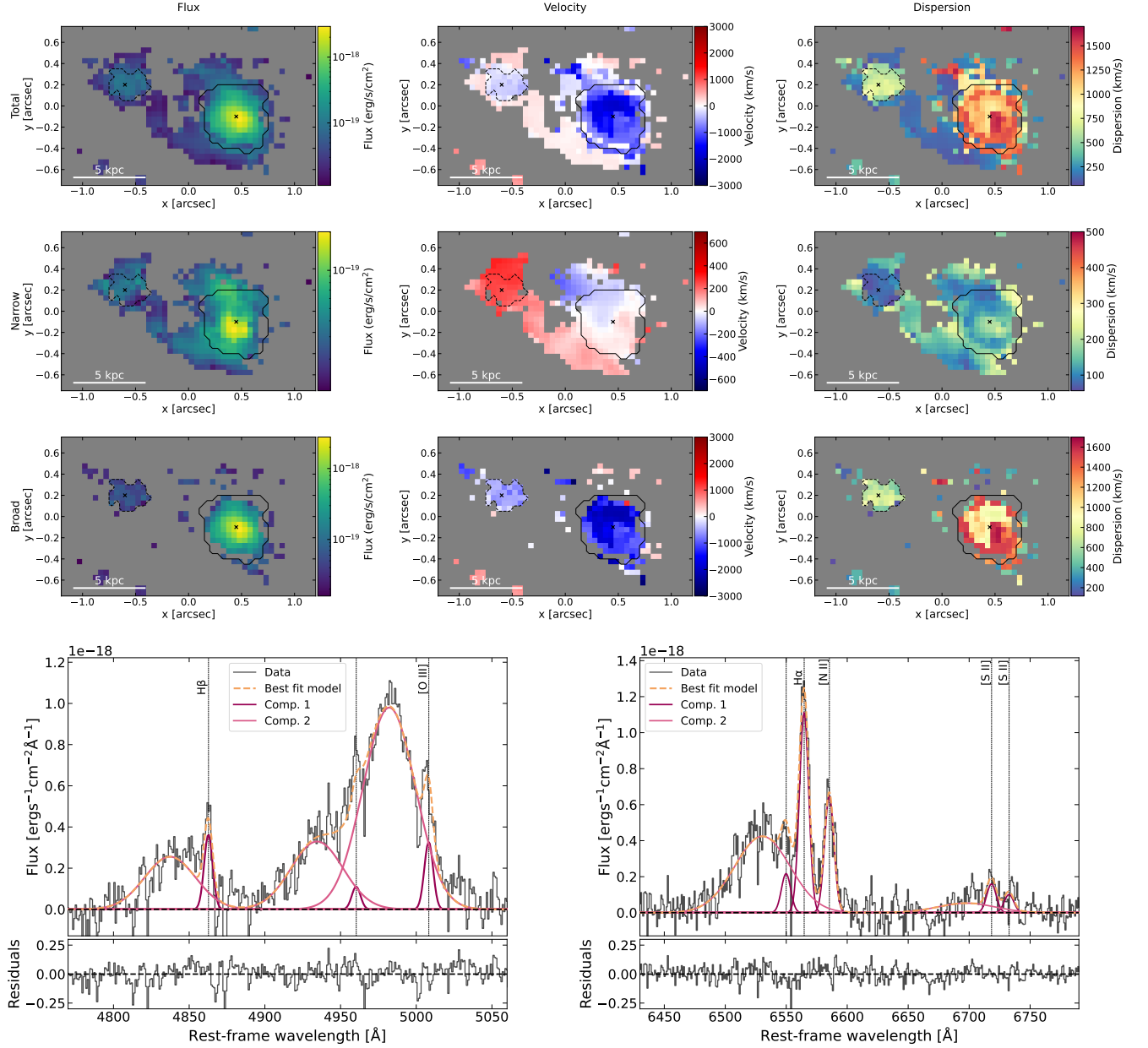


Fig. 3: *Top*: H α maps of COS1638 AGN A and B. From top to bottom: Total, narrow, and broad components. From left to right: Flux, velocity, and velocity dispersion. Solid (dashed) black contours mark the outflow region used to produce the outflow-integrated spectra of COS1638-A (COS1638-B). *Bottom*: Close-up on the H β + [O III] complex (left) and the H α + [N II] + [S II] complex (right) of the continuum- and BLR-subtracted spectrum of COS1638 AGN A integrated over the $S/N > 3$ mask of the broad [O III] emission at the position of AGN A (solid black line). Data and residuals are in black, total model is in dashed orange, single-line components are shown as dark to light purple. Component 1 corresponds to the narrow component; additional components add up to the broad component (component 2).

the highest S/N spaxels, corresponding to the emission peak at the target position. Having obtained the best model of the ionized gas emission, we separate narrow components, typical of systemic motions, from broader ones that are associated with peculiar, possibly disturbed, gas kinematics (“broad” component) in each spaxel. We identify as a narrow component those Gaussians with velocity shift $|\Delta v| < 300 \text{ km s}^{-1}$ and broadening $\sigma < 300 \text{ km s}^{-1}$, and flag as “broad” every other component not matching this requirement. Such thresholds roughly correspond to the expected rotation velocity and velocity dispersion for star-

forming galaxies of $\log(M_{\star}/M_{\odot}) \approx 10.5 - 11$ (e.g., see Förster Schreiber & Wuyts 2020, for a review).

We then produce the moment maps of order 0, 1 and 2 of the total model, the narrow component and the broad component(s) for each line included in the fitting process. We use the moment 0 maps of the broad component of H α and [O III] to characterize properties and size of the outflows in each target. Maps only show spaxels with $S/N > 3$, where the S/N is calculated based on the integrated flux over the $\pm 3\sigma$ velocity range of each line component. The systemic velocity used for the velocity maps is

given by the redshift estimated from the nuclear spectra and reported in Table 1.

4.2. Outflow-integrated spectra

To study the kinematic properties of outflows, we are interested in the characterization of the broad components of $H\alpha$ and [O III]. Yet, a proper characterization of other emission lines, like $H\beta$ and [S II], is necessary to measure all the needed physical quantities, for instance the density and temperature of the outflowing gas and the dust extinction of the outflow. Unfortunately, the strength of these other lines is not high enough to allow for a spatially resolved characterization of their emission in the outflow component. For this reason, we rely on spatially integrated spectra to measure some of the outflow properties.

We produce outflow-integrated spectra from the on-target 3σ mask of the [O III] or $H\alpha$ broad emission flux maps, depending on which of the two lines shows the most spatially extended broad component emission. For COS590, we exclude the spaxels at the position of the other components northern of the AGN ($\delta > 0.4''$ in Fig. A.6) because this emission is possibly associated to tidal tails and not outflows. Since wiggles are significant only at single-spaxel level and disappear when integrating over large-enough apertures, we extract integrated spectra from the datacubes that were not corrected for wiggles, to avoid any interpolation.

4.2.1. Fitting of the outflow-integrated spectra

Integrated spectra are fitted following the same steps used for cube fitting and described in Sect. 4.1. For Type 1 AGNi, we use the BLR template built in the cube-fitting process because it is less contaminated by large-scale, ionized-gas emission. We produce the ionized-gas integrated spectra by fitting and subtracting the continuum and, for Type 1 AGNi, the BLR component. We then fit the ionized-gas integrated spectra using from one to three Gaussian components, with velocity and width linked between the various emission lines. In contrast to the spaxel-by-spaxel approach, integrated spectra of COS1638-A and COS1638-B are well fitted by tying the Gaussian components between all the lines, further supporting the possibility of such asymmetries being due to an imperfect wiggles correction. We note that four Gaussian components are needed to best reproduce both the $H\alpha$ and the [O III] blue wings with linked kinematics between all the emission lines included in the fit (see Fig. A.3). We then select the best-fit model as the one with the lowest number of Gaussian components through the Kolmogorov-Smirnov test on the residual distribution. All spectra are best fitted using two or three Gaussian components. Figure 3 shows a close-up of the spectrum of COS1638-A around the [O III] and $H\alpha$ lines as an example, the spectra of the other targets are presented in Appendix A. We then identify the “narrow” component of each spectrum as the Gaussian component with velocity shift $|\Delta v| < 300 \text{ km s}^{-1}$ (with respect to the source rest frame) and broadening $\sigma < 300 \text{ km s}^{-1}$, and flag the remaining one or two Gaussian components as “broad”.

4.2.2. Dust extinction

We measure the extinction correction from the spectra integrated in the outflow region, that is, in the broad-component 3σ masks. The broad components of the $H\beta$ line, if any, are too faint and thus we do not estimate the extinction correction for the broad

components. We compute the Balmer decrements for the total model and for narrow components separately, for those spectra where the narrow components are well detected and decoupled from the other emission lines (that is, in COS1638-A, COS590 and COS1118). We use the extinction $v0.4.6$ python package (Barbary 2016) and the extinction law of Cardelli et al. (1989) with an intrinsic Balmer decrement $H\alpha/H\beta$ of 2.86. We estimate the uncertainty on $E(B-V)$ by propagating the uncertainty on the Balmer decrement.

Table 1 summarizes the measured dust extinction. As can be expected, we find Type 2 AGNi to be more extinguished than Type 1 AGNi. Only COS1118 and COS590, both Type 1 AGNi, allowed for the determination of dust extinction from both their total models and narrow components. However, while for COS1118 these two are consistent within errors, the total extinction measured in COS590 is lower than that derived from narrow components only. This could be due to the quality of the data or to an outflow that is overall less dust extinguished than the rest of the galaxy. Regarding the Type 2 AGNi, we find that COS1638-B is heavily extinguished ($A_V^{\text{tot}} = 4.2 \pm 0.8 \text{ mag}$) while COS1656-A presents a more moderate dust extinction ($A_V^{\text{tot}} = 2.2 \pm 0.9 \text{ mag}$). For COS349, the strong degeneracy between the BLR and NLR emission lines hampers a meaningful determination of its dust extinction. Such a degeneracy, even if less strong, is also present in COS1638-A, for which we could measure the dust extinction of the narrow components, that are well separated from the outflows, but not for the total model and for the broad components. For these two targets, we assume as dust extinction the median of the total extinction measured in the other two Type 1 AGNi of our sample, COS1118 and COS590. We note that dust extinction of the narrow component in COS1638-A is slightly higher than the median of the sample (see Table 1) but would lead to overall consistent results. Lastly, we consider as dust extinction of COS2949 the median of that measured in the other Type 2 AGNi of our sample (COS1638-B and COS1656-A) since its $H\beta$ line falls outside the NIRSpc wavelength range.

For all targets, we deredden the total measured fluxes using the dust extinction listed in Table 1. To correct for extinction the fluxes of the broad components, we use the dust extinction as derived for the total fluxes.

4.2.3. Gas density

The ratio of the [SII] $\lambda\lambda 6717, 6731$ lines is often used to estimate the electron density (e.g., Osterbrock & Ferland 2006; Cresci et al. 2023). Before the advent of JWST, the [S II] doublet could be observed only up to $z \approx 2.5$ with ground-based facilities. Unfortunately, [S II] emission of COS-AGNi is generally weak and is mostly undetected in single spaxels. In the spectra integrated over the outflow region, the [S II] doublet is undetected only in COS349. However, in the other targets the S/N of the [S II] doublet hampers any detection of blue wings like the prominent ones of the [O III] and $H\alpha$ lines (see Figs. A.4–A.9). For this reason, we fit the [S II] emission lines in the spectra integrated over the outflow region with a single Gaussian component to best measure the [S II] line ratio and convert it to gas density following Osterbrock & Ferland (2006). We do it in two ways: *i*) we fit the [S II] lines alone with one Gaussian component each without linking their velocity parameters to the other lines, and *ii*) we used one Gaussian component with velocity shift and broadening set to those of the narrow component of the bright lines. We find that the two methods yield consistent results for all targets but COS1638-A and COS2949. In fact, these two AGNi are the

only ones that show broader and blueshifted emission in the [S II] lines (see Figs. 3 and A.9 for COS1638-A and COS2949, respectively); however, they do not share velocity shift and broadening of the outflows in the bright lines as an effect of the lower S/N. We thus fit the [S II] lines of these two AGNi with two Gaussian components, for both fitting methods described above. Yet, as an effect of the degeneracy intrinsic to using a total of four Gaussian components to fit the low S/N [S II] lines, the yielded best models include a broad component only in one of the two [S II] lines, leading to an unphysical determination of the [S II] ratio in the broad components and precluding the determination of the electron density of the outflows.

In all cases, the [S II] ratio uncertainties are large and in some cases span the full density range the [S II] ratio is sensitive to. For this reason, here we only quote the density regime of our targets following Osterbrock & Ferland (2006). The [S II] ratio range of COS2949 and COS1656-A indicates gas in a high density regime ([S II] $\lambda\lambda 6717, 6731 \lesssim 0.6$, i.e., $n_e \gtrsim 3300 \text{ cm}^{-3}$); the [S II] ratios of COS1118 and COS590 indicate gas in a low density regime ([S II] $\lambda\lambda 6717, 6731 \gtrsim 1.2$, i.e., $n_e \lesssim 200 \text{ cm}^{-3}$); within the uncertainties, the [S II] ratio of COS1638-A and -B covers the full density range the [S II] ratio is sensitive to, even though at face value COS1638-B might host more dense gas ($n_e \approx 1000 \text{ cm}^{-3}$) than COS1638-A ($n_e \approx 260 \text{ cm}^{-3}$).

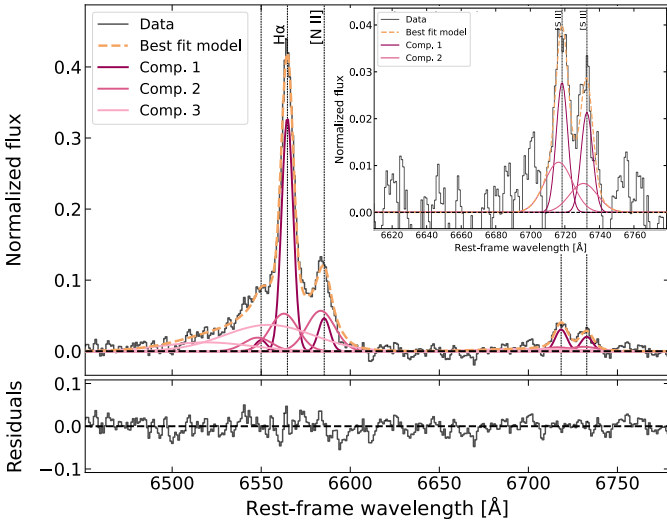


Fig. 4: Fit of stack spectrum. Data and residuals are in black, the total model is in dashed orange, and single line components are shown as dark to light purple. Inset: Close-up on the [S II] emission lines. The color coding is as in the main figure.

With the aim of increasing the S/N on the [S II] lines, we also analyze the spectrum obtained by stacking all COS-AGNi targets, except for COS349 because undetected in the [S II] lines. We weigh each BLR- and continuum-subtracted spectrum integrated over the outflow region on its errors, we normalize each weighted spectrum to the peak of the [S II] $\lambda 6717 \text{ Å}$ emission line before stacking and then we normalize the stack spectrum to its peak. We fit $H\alpha$, [N II] and [S II] lines in the normalized stack spectrum using three Gaussian components with linked velocity dispersion and shift (see Fig. 4). The [S II] line ratio in the stack spectrum is typical of gas in the low density regime ([S II] $\lambda\lambda 6717, 6731 \gtrsim 1.2$, $n_e \lesssim 200 \text{ cm}^{-3}$), both for the narrow and the broad Gaussian components. A similar result is obtained also when allowing the [S II] line ratio to vary only in the 0.4-1.4

range, that is, excluding the asymptotic regimes where the [S II] ratio becomes insensitive to gas density variations.

In summary, we find that the [S II] ratio of COS2949, COS1656-A and COS1638-B indicates a high density regime for the bulk of the gas in the galaxy ($n_e \gtrsim 3300 \text{ cm}^{-3}$ in the first two, $n_e \approx 1000 \text{ cm}^{-3}$ in the third), while the [S II] ratio of COS1118, COS590 and COS1638-A is indicative of a global low electron density ($n_e \lesssim 260 \text{ cm}^{-3}$). These results might hint to Type 2 AGNi harboring denser gas compared to Type 1 AGNi, yet our sample size is small and the [S II] ratio of COS1638-A and -B becomes consistent to the full density range the [S II] ratio is sensitive to considering the uncertainty range. Results from the stack spectrum indicate a global electron density of $n_e \lesssim 200 \text{ cm}^{-3}$ for both narrow and broad components of the [S II] emission lines. However, we did not observe in the [S II] lines of the stack spectrum the same prominent blueshifted components shown by $H\alpha$. We thus consider our results from the stack as indicative of the global mean electron density of COS-AGNi, which is likely dominated by sources in the low density regime and affected by a fitting degeneracy between narrow and broad components, but not as representative of the density within the prominent outflows observed in our targets.

5. Results

We present the line ratios and diagnostic diagrams in Sect. 5.1, discuss the properties of single sources in Sect. 5.2 and compute the physical properties of the outflows in Sect. 5.3. Full spectra are shown in Fig. A.1-A.3, while maps and close-up spectra in the $H\beta$ + [O III] and $H\alpha$ + [N II] regions are shown in Fig. A.4-A.9.

5.1. Diagnostic diagrams

First, we produce diagnostic diagrams to inspect the ionization nature of the total, narrow (i.e., systemic) and broad (i.e., outflow) components. We employ both standard optical diagnostic diagrams (BPT and VO87 diagrams; e.g., Baldwin et al. 1981; Veilleux & Osterbrock 1987; Kewley et al. 2013), and the novel diagnostics suggested by Mazzolari et al. (2024). Figure 5 shows the following diagnostic parameter spaces: *i*) $\log([O \text{ III}]\lambda 5007/H\beta)$ versus $\log([N \text{ II}]/H\alpha)$; *ii*) $\log([O \text{ III}]\lambda 5007/H\beta)$ versus $\log([S \text{ II}]/H\alpha)$; *iii*) $\log([O \text{ III}]\lambda 4363/H\gamma)$ versus $\log([O \text{ III}]\lambda 5007/[O \text{ II}]\lambda 3727)$; *iv*) $\log([O \text{ III}]\lambda 4363/H\gamma)$ versus $\log([Ne \text{ III}]\lambda 3869/[O \text{ II}]\lambda 3727)$ ⁷; *v*) $\log([O \text{ III}]\lambda 4363/H\gamma)$ versus $\log([O \text{ III}]\lambda 5007/[O \text{ III}]\lambda 4363)$. We plot line ratios as measured from the spectra integrated over the outflow region of all the AGNi for which the needed emission lines are detected in the total, narrow and broad components (see Figs. A.4-A.9 and A.3). We exclude COS1638-A and COS349 because of the strong degeneracy between the BLR and NLR line components due to strong broad Balmer lines (see also Perna et al. 2025b).

All AGNi that allow for the computation of the line ratios needed for the diagnostic diagrams fall in the AGN region (see Fig. 5). We note that also the outflow components for which the line ratios can be computed fall in the AGN region, as expected for outflows driven by AGNi. COS1118, COS590 and COS1656-A show the needed lines for the diagnostic diagrams presented in Mazzolari et al. (2024), providing further proof of the validity of the [O III] $\lambda 4363 \text{ Å}$ diagrams in discerning AGNi

⁷ [O II] $\lambda 3727$ refers to the sum of [O II] $\lambda\lambda 3726, 3728$ as in Mazzolari et al. (2024).

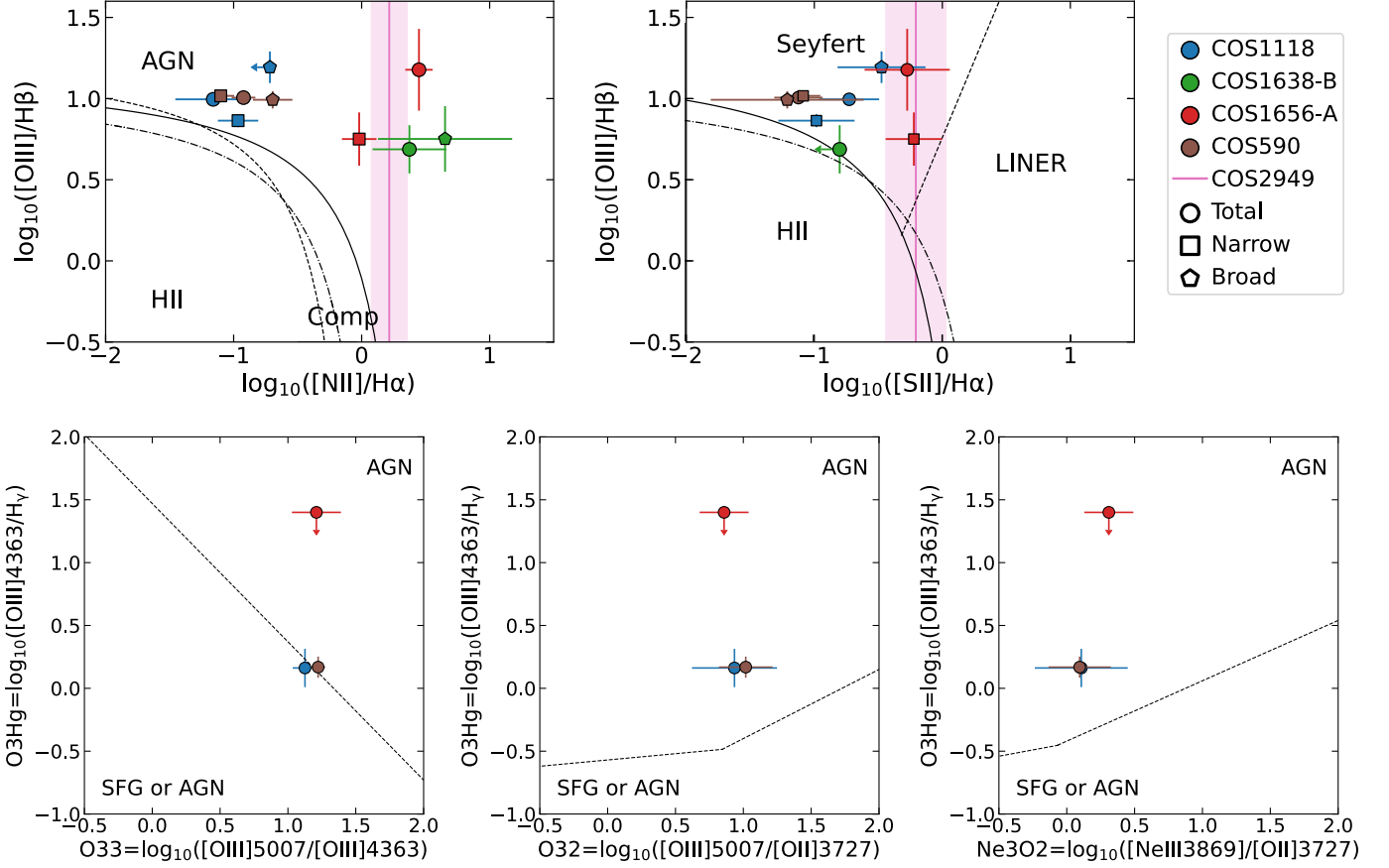


Fig. 5: Diagnostic diagrams. *Top, left to right*: Standard optical $\log([\text{O III}]/\text{H}\beta)$ versus $\log([\text{N II}]/\text{H}\alpha)$ and $\log([\text{O III}]/\text{H}\beta)$ versus $\log([\text{S II}]/\text{H}\alpha)$ diagnostic diagrams. Different ionization regimes are separated by solid and dashed black lines, taken from Kewley et al. (2001, 2006) and Kauffmann et al. (2003). Dashed-dotted black lines show the observed position of $z \approx 2 - 3$ star-forming galaxies in Strom et al. (2017). *Bottom, left to right*: Diagnostic diagrams $\log([\text{O III}]\lambda 4363/\text{H}\gamma)$ versus $\log([\text{O III}]\lambda 5007/[\text{O III}]\lambda 4363)$, $\log([\text{O III}]\lambda 4363/\text{H}\gamma)$ versus $\log([\text{O III}]\lambda 5007/[\text{O II}]\lambda 3727)$, and $\log([\text{O III}]\lambda 4363/\text{H}\gamma)$ versus $\log([\text{Ne III}]\lambda 3869/[\text{O II}]\lambda 3727)$ and demarcation lines from Mazzolari et al. (2024). Total, narrow, and outflow component line fluxes are shown as circles, squares, and pentagons. COS2949 is marked as a pink line since NIRSpect/IFU data do not cover the $\text{H}\beta + [\text{O III}]$ range. Error bars are dominated by the uncertainties resulting from extinction correction.

and star forming galaxies. Standard line ratios are known to vary with redshift and JWST results have recently highlighted how the standard diagnostic diagrams fail to identify high- z AGNi residing in low-mass and low-metallicity host galaxies, often missing X-ray emission (e.g., Sanders et al. 2023; Shapley et al. 2025). However, such an effect does not apply to our sources. The AGNi analyzed in the present work were selected in the X-rays for showing $L_{2-10} > 10^{44} \text{ erg s}^{-1}$, that is, as “standard” AGNi, and thus their position in both the BPT and VO87 optical diagnostic diagrams and in those of Mazzolari et al. (2024) is in line with expectations. Lastly, we note that COS-AGNi reside in galaxies that are massive and close to the main sequence of star forming galaxies (see Fig. 1, right) and are not placed at such a high redshift to be expected to be metal poor (unlike other GA-NIFS AGNi, for instance GS_3073 presented in Übler et al. 2023).

5.2. Notes on individual sources

COS1118. This target is a Type 1 AGN at $z = 3.643$ (Trump et al. 2009; Brusa et al. 2009), as confirmed by this work. The

target is unobscured in the X-rays and shows a rest-frame 2–10 keV luminosity $L_{2-10} \approx 3 \times 10^{44} \text{ erg s}^{-1}$ (Marchesi et al. 2016). NIRSpect/IFU spectra of COS1118 are rich in emission lines, including nebular lines such as $[\text{O II}]\lambda\lambda 3726, 3728$, $\text{H}\gamma$, $\text{H}\delta$, $[\text{Ne III}]\lambda 3869\text{\AA}$, $[\text{O III}]\lambda 4363\text{\AA}$ and $\text{He II}\lambda 4687\text{\AA}$. However, many of these lines are detected only in a few spaxels of the cube and therefore do not allow for a spatially resolved analysis. Nevertheless, they are well seen in the integrated spectra (see Fig. A.1), thus enabling computation of the line ratios needed for the diagnostic diagrams in Fig. 5. This target shows spatially extended narrow emission both in the $\text{H}\alpha$ and $[\text{O III}]$ lines (see Fig. A.4 for the $[\text{O III}]$ line). The North-West region shows ionized gas that is detected in both lines, sharing similar blueshifted kinematics in their narrow components, while redshifted emission extending South-East of the target is present only in the $[\text{O III}]$ line, without a counterpart in $\text{H}\alpha$. The total extent of the $[\text{O III}]$ nebula is slightly less than $2''$ in major axis, corresponding to $\lesssim 15$ kpc, while the $\text{H}\alpha$ emission is much less extended ($\approx 0.7''$ in major axis, corresponding to ≈ 5 kpc). Emission from perturbed gas, traced by the outflow components, is much less extended and detected only in the proximity of the AGN (within

0.5'' both in [O III] and $H\alpha$). The integrated spectrum in the outflow region is dominated by the gas at rest with the galaxy, yet broad components are needed to reproduce the broad line wings visible both in the [O III] and $H\alpha$ lines and in all the brighter lines (see Fig. A.4). The kinematic properties of the ionized nebula are thus not clearly linked to the outflow detected in this AGN and more data would be needed to probe its origin. Unfortunately, no other spatially resolved data are available in the archives (e.g., ESO, ALMA, VLA) for this target, thus hampering a more detailed study of this [O III]-traced nebula.

COS349. This target is a Type 1 AGN (redshift measured with VLT/VIMOS: $z = 3.5078$, Lilly et al. 2007) at $z = 3.5093 \pm 0.0003$ (as measured in this work) that is unobscured in the X-rays and shows a rest-frame 2–10 keV luminosity $L_{2-10} \approx 1.8 \times 10^{44} \text{ erg s}^{-1}$ (Marchesi et al. 2016). The rest-frame optical properties of COS349 were first analyzed in Trakhtenbrot et al. (2016), focusing on the BLR properties and SMBH mass derivation, through low-S/N Keck/MOSFIRE K-band spectra (alias of source ID: CID-349) covering only the $H\beta$ + [O III] complex. No outflow component was detected by Trakhtenbrot et al. in the [O III] lines, probably due to the lower spectral resolution and lower S/N and to an overestimated contribution from Fe II owing to the limited rest-frame wavelength range covered by the MOSFIRE spectrum ($\approx 4500 - 5200 \text{ \AA}$). JWST/NIRSpec IFU data show the presence of prominent Fe II emission as well as complex and perturbed kinematics suggested by the need of multiple Gaussian components (see Fig. A.2). Emission line maps show a compact structure for the ionized gas in this AGN, which is the most compact observed in the GA-NIFS AGNi sample (roughly 3.5 kpc in diameter), both in the narrow and in the broad gas components, as can be seen from the maps in Figs. 2 and A.5. Degeneracy between BLR and NLR components is strong, likely producing an oversubtraction of the BLR component of the $H\beta$ line (Fig. A.5) and strong degeneracy between $H\alpha$ and [N II] in the fitting of the spectrum integrated in the outflow region. For this reason, we do not include this target in the diagnostic diagrams and compute its mass outflow rate using also the [O III] emission line, in addition to the $H\alpha$ line (see Sect. 5.3).

COS590. This target is a Type 1 AGN at $z = 3.52385$ (previous redshift $z = 3.535 \pm 0.013$, Trump et al. 2009) that could be partially obscured in the X-rays ($N_H < 1.6 \times 10^{23} \text{ cm}^{-2}$) and shows a rest-frame 2–10 keV luminosity $L_{2-10} \approx 2.6 \times 10^{44} \text{ erg s}^{-1}$ (Marchesi et al. 2016). COS590 presents a clumpy morphology, with at least two companions at slightly higher redshift than the central AGN, as traced by the redshifted emission to the north of the AGN in Fig. A.6. All the components are well traced by both [O III] and $H\alpha$ narrow emission lines ($|\nu| < 300 \text{ km/s}$, $\sigma < 300 \text{ km/s}$), with brighter emission in the [O III] line. Continuum emission is also present in these additional components and the elongated morphology of COS590 suggests an ongoing merger. Moreover, the additional components do not show broad wings in the Balmer lines and are undetected in both [S II] and [N II], thus we have no means to discriminate between SFGs or AGNi. A more in-depth analysis of the other components and diffuse emission is outside the scope of the present paper. However, as for COS1118, no other spatially resolved data are available for this system, hampering a multiwavelength characterization of the companions revealed by NIRSpec/IFU. The central AGN shows broad emission at its core and in its proximity, with [O III]-traced gas bridging the AGN and the closest companion.

Broad [O III] emission is also detected in a few spaxels close to the position of one of the northern clumps. The integrated spectrum in the outflow region (i.e., the black contour enclosing the AGN in the broad emission map of Fig. A.6) exhibits prominent narrow emission and a blueshifted broad component that is present in all the brightest emission lines.

COS1638-A and -B. This target is a Type 1 AGN (redshift from the SDSS quasar catalog: $z = 3.5026$, Pâris et al. 2014) at $z = 3.5057$ (as measured in this work) that could be partially obscured in the X-rays ($N_H < 3.2 \times 10^{23} \text{ cm}^{-2}$) and shows a rest-frame 2–10 keV luminosity $L_{2-10} \approx 2.6 \times 10^{44} \text{ erg s}^{-1}$ (Marchesi et al. 2016). The $H\beta$ + [O III] complex of COS1638 was analyzed in Trakhtenbrot et al. (2016), focusing on the BLR properties, through a low-S/N Keck/MOSFIRE K-band 1-D spectrum (alias of source ID: LID-1638). Prominent [O III] asymmetric lines are visible also in the MOSFIRE spectrum, which the authors interpreted as possibly due to prominent outflows or as indicative of a dual AGN candidate. JWST/NIRSpec IFU indeed confirms the presence of extremely prominent blueshifted outflows, as argued by the Trakhtenbrot et al.. The exquisite sensitivity of JWST/NIRSpec data also allowed Perna et al. (2025b) to identify COS1638 as a dual AGN: COS1638-A is a Type 1 AGN at $z = 3.5057$, while its companion, COS1638-B, is a type 2 AGN at $z = 3.5109$. Given the similarity of the MOSFIRE spectrum with that of COS1638-A (Trakhtenbrot et al. 2016), it is likely that COS1638-B was not in the MOSFIRE slit. Both targets are brighter in $H\alpha$ than in the [O III] line and both their nuclear spectra and those integrated over the outflow region are dominated by very broad emission lines tracing prominent outflows and highly perturbed gas kinematics (see Figs. 3, A.2 and A.7). Both AGNi are also characterized by extended emission in $H\alpha$, whose narrow component bridges the two AGNi (Figs. 2 and 3). The [O III] emission from COS1638-A shows an extension with a C-shape structure, with an arm extending toward COS1638-B, yet without connecting the two (see Figs. 2 and A.7). The emission around the positions of both AGNi in this dual system is characterized by extremely broad [O III] emission lines that are much more prominent than the gas at rest in the galaxy (Figs. 3 and A.7, for spectra of COS1638-A and -B, respectively). In fact, the total emission of both AGNi is completely dominated by blueshifted gas at $\nu < -1000 \text{ km s}^{-1}$, while the narrow component is almost undetectable at the spaxel level, probably too weak and thus drowned in the prominent outflow component. These peculiar spectral shapes are also observed in the sub-millimeter galaxy companion of BR1202-0725 at $z \approx 4.7$ (Zamora et al. 2024).

COS1656-A. This target is a Type 2 AGN with a rest-frame 2–10 keV luminosity $L_{2-10} \approx 2.7 \times 10^{44} \text{ erg s}^{-1}$ at $z = 3.5101$ (as measured in this work and roughly consistent with the redshift $z = 3.512$ from the COSMOS collaboration, Marchesi et al. 2016; Hasinger et al. 2018) and for which obscuration in the X-rays could not be measured in COSMOS-Legacy (Marchesi et al. 2016). NIRSpec/IFU data of COS1656 recently allowed Perna et al. (2025b) to resolve the target into a dual system (projected separation of 1.4'' corresponding to $\approx 10 \text{ kpc}$), with both sources identified as Type 2 AGN. COS1656-B probably has a close galaxy companion that contaminates its emission, and as such we left it out of our analysis due to the impossibility of disentangling emission of the companion from possible broad components in the spectrum of AGN-B. COS1656-A shows extended ionized gas traced in both $H\alpha$ and [O III] narrow and broad emis-

Table 2: Outflow properties of the GA-NIFS COS-AGNi sample as traced by the H α emission line.

Target	$L_{\text{H}\alpha, \text{out}}$ (10^{41} erg s $^{-1}$)	$R_{\text{out, fw}}$ (kpc)	v_{out} (km s $^{-1}$)	M_{out} ($10^6 M_{\odot}$)	\dot{M}_{out} (M_{\odot} yr $^{-1}$)	\dot{E}_{out} (10^{41} erg s $^{-1}$)	R_{max} (kpc)	v_{max} (km s $^{-1}$)
(1)	(2)	(3)	(4)	(5)	(6)	(7)	(8)	(9)
COS590	12.1 \pm 0.2	1.0 \pm 0.4	569 \pm 9	3.9 \pm 1.9	6.6 \pm 4.1	6.8 \pm 4.2	2.6 \pm 0.7	796 \pm 5
COS1118	6.3 \pm 0.2	0.7 \pm 0.4	707 \pm 4	2.0 \pm 1.0	5.9 \pm 4.1	9.3 \pm 6.5	2.6 \pm 0.7	823 \pm 3
COS349	7.9 \pm 0.4	1.0 \pm 0.4	1278 \pm 13	2.5 \pm 1.3	10.4 \pm 6.6	53.5 \pm 34.2	2.6 \pm 0.7	1384 \pm 8
COS1656-A	18.4 \pm 1.6	1.2 \pm 0.4	950 \pm 9	5.9 \pm 3.0	14.8 \pm 8.9	42.2 \pm 25.4	2.6 \pm 0.7	1326 \pm 6
COS2949	5.7 \pm 0.1	1.0 \pm 0.4	732 \pm 5	1.8 \pm 0.9	4.3 \pm 2.9	7.3 \pm 4.9	2.1 \pm 0.9	901 \pm 3
COS1638-A	33.9 \pm 0.3	0.9 \pm 0.4	3199 \pm 201	10.9 \pm 5.4	120.8 \pm 79.7	3900.8 \pm 2676.5	3.0 \pm 0.7	3551 \pm 131
COS1638-B	307.3 \pm 0.9	1.1 \pm 0.4	2066 \pm 90	98.3 \pm 49.2	568.0 \pm 345.0	7652.3 \pm 4754.5	1.8 \pm 0.7	2623 \pm 56

Notes. Outflow properties in columns (5) to (7) are computed with flux-weighted outflow radii, outflow velocity $v_{\text{out}} = \max(v_{10}, v_{90})$ and $n_e = 1000 \text{ cm}^{-3}$. The last two columns list the parameters needed to scale the outflow properties to the framework used for the comparison with the literature. Columns: (1) target name; (2) H α luminosity in units of $10^{41} \text{ erg s}^{-1}$; (3) flux-weighted outflow radius in kpc units; (4) outflow velocity $v_{\text{out}} = \max(v_{10}, v_{90})$ in km s $^{-1}$; (5) outflow mass computed from Eq. 2 in units of solar masses; (6) mass outflow rate computed in biconical geometry (Eq. 4) in units of solar masses per year; (7) outflow kinetic power in units of $10^{41} \text{ erg s}^{-1}$; (8) maximum outflow radius in kpc units; (9) maximum outflow velocity $v_{\text{max}} = |v_{\text{nar}} - v_{\text{bro}}| + 2\sigma_{\text{bro}}$ in km s $^{-1}$.

sion lines (see Fig. A.8 for the [O III] maps). Interestingly, the narrow components of both lines seem to trace the core of the AGN host and a close by clump South-East of COS1656-A characterized by blueshifted emission with lower velocity dispersion compared to the AGN host. Such a clump is also clearly visible in the three-color images maps of Fig. 2. However, the broad components of both H α and [O III] only partially involve such a clump as they both mostly extend North-East of COS1656-A (Fig. A.8).

COS2949. This target is a Type 2 AGN that was included in the GA-NIFS program because it is listed as a $z \approx 3.5$ AGN in the COSMOS-Legacy catalog, based on a spectroscopic redshift ($z = 3.571$ estimated from a VIMOS spectrum Marchesi et al. 2016). Yet, NIRSpect observations revealed that COS2949 is definitely a lower redshift source: NIRSpect/IFU data only shows the H α complex in its bluest side, and its wavelength range ends redward of the [O III] emission line. We estimate the new redshift as $z = 2.0478$, which is much more similar to the photometric redshift of the COSMOS-Legacy catalog ($z \approx 2.55$; Marchesi et al. 2016). We thus recomputed the X-ray properties of COS2949 at the redshift measured with JWST (see Table 1). The AGN associated with the X-ray emission detected in COSMOS-Legacy corresponds to the only source of this NIRSpect field emitting in [N II], traced in both its narrow and broad components, and in continuum (see Fig. 2). Such an AGN is surrounded by at least one H α -emitting companion in the South-East direction (projected separation $0.7''$ corresponding to ≈ 6 kpc) and by other clumps traced by narrow, low-dispersion H α emission (see Fig. A.9). The AGN itself is dominated by blueshifted ($v < -350$ km/s), large-dispersion ($\sigma > 300$ km/s) emission in its Southern side, that is, the one toward the brightest companion, and narrow, lower-dispersion emission in the Northern side, that is, connected to a receding H α -emitting gas stream.

5.3. Outflow properties

We compute the physical properties of the outflows in GA-NIFS COS-AGNi using the H α emission line to avoid the additional assumptions regarding gas metallicity. For instance, using the [O III] emission line as tracer of ionized gas mass in AGNi outflows was found to produce a factor 2–3 \times lower mass outflow rates (e.g., Cano-Díaz et al. 2012; Carniani et al. 2015; Cresci et al.

2023; Venturi et al. 2023). Given the degeneracy of BLR and NLR components in COS349, for this target we derive the mass outflow rate also from the [O III] emission line and discuss the possible differences.

5.3.1. Outflow gas density

As discussed in Sect. 4.2.3, our data do not allow us to measure the gas density in a spaxel-by-spaxel way and the gas densities estimated from the spectra integrated over the outflow region should be considered as representative of the total system. The majority of COS-AGNi show a total gas density of $n_e \lesssim 200 \text{ cm}^{-3}$, with two targets having much higher density ($n_e \gtrsim 3300 \text{ cm}^{-3}$). As a result, the density that can be measured from the [S II] line ratio in the stack spectrum is dominated by the contribution of the targets showing a lower gas density ($n_e \lesssim 200 \text{ cm}^{-3}$). In any case, the quality of the data did not allow for the density of the outflow to be measured.

At the redshift of our AGNi, few other sources have electron density measurements (Isobe et al. 2023; Cresci et al. 2023; Marconcini et al. 2024; Li et al. 2024), two of which are star-forming galaxies part of the GA-NIFS sample (Lamperti et al. 2024; Rodríguez Del Pino et al. 2024). Galaxies at $z \approx 3 - 4$ show a median gas density of $200 - 300 \text{ cm}^{-3}$, and thus the tentative measurements from our work are roughly consistent with results in the literature. However, these values are referred to gas at rest in star-forming galaxies and it is reasonable to expect outflows, especially if AGN driven, to be denser, as found at lower redshift (e.g., Perna et al. 2017; Förster Schreiber et al. 2019). Other works focusing on AGN-driven outflows have found a variety of results (e.g., Mingozzi et al. 2019; Förster Schreiber et al. 2019; Davies et al. 2020a; Cresci et al. 2023; Speranza et al. 2024), with values ranging from few hundreds to few thousands of atoms per cm 3 . Here we assume an outflow gas density of $n_e = 1000 \text{ cm}^{-3}$ with a 50% uncertainty to best consider the available measurements at cosmic noon, which mainly come from the KMOS 3D survey (Förster Schreiber et al. 2019).

5.3.2. Outflow radius

We estimate the outflow radius in two ways. First, we take advantage of the spatially resolved maps available for our sample and

compute the flux-weighted outflow radius ($R_{\text{out,fw}}$) as follows:

$$R_{\text{out,fw}} = \frac{\sum_{i,j} d(X_{\text{peak}}, X_{i,j}) f_{i,j}^{\text{broad}}}{\sum_{i,j} f_{i,j}^{\text{broad}}}, \quad (1)$$

where $d(X_{\text{peak}}, X_{i,j})$ is the distance between the peak of the total line flux of a target (X_{peak}) and the spaxels with $S/N > 3$ broad component emission ($X_{i,j}$), and $f_{i,j}^{\text{broad}}$ is the flux of the broad component in the corresponding spaxel. Secondly, we also measure the maximum outflow radius $R_{\text{out,max}}$ as the maximum distance between the flux peak and the furthest spaxel showing broad emission at $S/N > 3$ to compare our results with those of the literature, in particular to [Fiore et al. \(2017\)](#) and later works employing the same framework. In few of our targets, the $\text{H}\alpha$ line shows a lower overall S/N in the maps compared to the [O III] line. We thus estimated the spatial extension of the outflow as the maximum between that observed in $\text{H}\alpha$ and [O III], or $\text{H}\alpha$ and [N II] for COS2949 given the unavailability of the [O III] line. We correct both the flux-weighted radius and the maximum radius of the outflows by subtracting the PSF FWHM/2 in quadrature, using the modeling of NIRSpec PSF FWHM as in [D'Eugenio et al. \(2024\)](#). We note that the extension of the outflows measured as flux-weighted radii ($R_{\text{out,fw}} \approx 0.1'' - 0.16''$) is roughly twice the PSF FWHM and that the maximum radial extent ($R_{\text{max}} \approx 0.25'' - 0.4''$) is at least $2.5\times$ the PSF.

5.3.3. Mass outflow rate and kinetic power

We computed the $\text{H}\alpha$ outflow mass assuming an electron temperature of $T_e \approx 10^4$ K, typical of optically emitting warm ionized gas, and applying the formula from [Cresci et al. \(2017\)](#):

$$M_{\text{out}}(\text{H}\alpha) = 3.2 \times 10^5 \frac{L_{[40]}(\text{H}\alpha)}{n_{\text{e}[2]}} M_{\odot}, \quad (2)$$

where $L_{[40]}(\text{H}\alpha)$ is the dereddened $\text{H}\alpha$ luminosity of the outflow (see Sect. 4.2.2) in units of 10^{40} erg s^{-1} and $n_{\text{e}[2]}$ is the outflow gas density in units of 10^2 cm^{-3} . As mentioned, for COS349, we computed the [O III] outflow mass following [Cano-Díaz et al. \(2012\)](#) and again assumed an electron temperature of $T_e \approx 10^4$ K:

$$M_{\text{out}}([\text{OIII}]) = 5.33 \times 10^7 \frac{C L_{[44]}([\text{OIII}])}{n_{\text{e}[3]} 10^{[\text{O/H}]/[\text{O/H}]_{\odot}}}. \quad (3)$$

Here, $L_{[44]}([\text{OIII}])$ is the dereddened [O III] luminosity of the outflow (see Sect. 4.2.2) in units of 10^{44} erg s^{-1} , $n_{\text{e}[3]}$ is the outflow gas density in units of 10^3 cm^{-3} , C is the condensation factor that we assumed is equal to one (i.e., we assumed that all ionizing gas clouds have the same density), and $10^{[\text{O/H}]/[\text{O/H}]_{\odot}}$ gives the oxygen abundance in solar units that we assumed as solar.

None of the COS-AGNi allow the outflow geometry to be resolved. We then computed the mass outflow rate assuming a biconical outflow geometry considering recent works both at low redshift (e.g., [Musiimenta et al. 2023](#); [Zanchettin et al. 2023](#)) and high-redshift (e.g., [Kakkad et al. 2020](#); [Tozzi et al. 2024](#)):

$$\dot{M}_{\text{out}}^{\text{cone}} = 3M_{\text{out}} \frac{v_{\text{out}}}{R_{\text{out}}}, \quad (4)$$

with $v_{\text{out}} = \max(v_{10}, v_{90})$ (e.g., [Tozzi et al. 2024](#)), where v_{10} and v_{90} are the 10th and 90th percentiles of the velocity line profile of the broad $\text{H}\alpha$, R_{out} is the flux-weighted radius $R_{\text{out,fw}}$ from Eq. 1, and the factor 3 corresponds to the assumption of a constant average volume density in the cone (e.g., [Lutz et al. 2020](#)). We

estimate the uncertainty of v_{out} as the standard deviation of the mean of its spatially resolved maps from cube-fitting results, restricted to the spaxels above 3σ in the broad flux map and having excluded the spaxels associated to random noise. We note that this procedure returns a larger uncertainty for the outflow velocity in COS1638-A, due to the very large velocity values in each spaxel, ranging from $\gtrsim 2000 \text{ km s}^{-1}$ up to $\approx 3500 \text{ km s}^{-1}$. We consider one spaxel of uncertainty ($0.05''$) for the flux-weighted radius, that translates to $\approx 0.4 \text{ kpc}$ at $z \approx 3.5$. We then compute the kinetic power \dot{E}_{out} of the outflows as $\dot{E}_{\text{out}} = \frac{1}{2} \dot{M}_{\text{out}} v_{\text{out}}^2$.

Table 2 summarizes the outflow properties derived from $\text{H}\alpha$ and computed with $v_{\text{out}} = \max(v_{10}, v_{90})$, $R_{\text{out}} = R_{\text{out,fw}}$ and $n_e = 1000 \text{ cm}^{-3}$. For COS349, we obtained $M_{\text{out}}([\text{OIII}]) = (3.0 \pm 1.5) \times 10^5 M_{\odot}$, that is roughly one order of magnitude lower than the value measured from the $\text{H}\alpha$ broad emission component. This could be indicative of an overestimation of the $\text{H}\alpha$ broad component in the best fit of the ionized-gas spectrum (see Fig. A.5) or of wrong assumptions in our computation of the outflow mass. For instance, Eq. 3 assumes a temperature of $T \approx 10^4$ K, typical of NLR, for which the emissivity of the [O III] has a weak dependence on the temperature. Moreover, one of the strongest assumptions behind Eq. 3 is that most of oxygen in the ionized outflow is in the form O^{2+} . Lastly, it could also be due to a wrong estimation of the dust reddening in COS349. In fact, due to the strong degeneracy between BLR and NLR lines, we could not estimate the Balmer decrement of this target, and thus we used the median of the other Type 1 AGNi of our sample. We note that the outflow velocity estimated from [O III] and from $\text{H}\alpha$ for this target are consistent with each other. Thus, any difference in the outflow properties originates from the outflow mass determination.

For a consistent comparison with literature results in Sect. 6, in particular with the L_{bol} versus v_{max} , \dot{M}_{out} versus L_{bol} and \dot{E}_{out} versus L_{bol} scaling relations of [Fiore et al. \(2017\)](#) and [Musiimenta et al. \(2023\)](#), we re-compute the outflow energetics with the definition of outflow velocity and extent as adopted by those authors. In particular, we use $v_{\text{max}} = |v_{\text{nar}} - v_{\text{bro}}| + 2\sigma_{\text{bro}}$ (as defined in [Rupke & Veilleux 2013](#)) as the outflow velocity and the maximum extension of the outflow as radius (R_{max}). We estimate v_{bro} and σ_{bro} as the moment 1 and moment 2 of the $\text{H}\alpha$ broad line profile and v_{nar} as the moment 1 of the $\text{H}\alpha$ narrow line profile in the outflow spectra, and compute their uncertainties as the spaxel-by-spaxel standard deviation of such parameters in the spatially resolved cube fitting, as done for v_{out} . We measure the maximum radius R_{max} of the outflow as the maximum distance of the broad component emission from the AGN in the 3σ flux maps. We assign to R_{max} an uncertainty of 2 spaxels, i.e., $0.1''$, to take into account the asymmetrical extension of the broad emission. We then compute the mass outflow rate assuming a biconical outflow geometry (Eq. 4). Table 2 also summarizes the parameters used to recompute the outflow properties following the assumptions of [Fiore et al. \(2017\)](#), which are the maximum outflow velocity v_{max} and the outflow maximum extension R_{max} .

6. Discussion

The GA-NIFS COS-AGNi are among the first targets having spatially resolved, rest-frame optical observations of AGNi outflows at $z > 3$ in the luminosity range $\log(L_{\text{bol}}/\text{erg s}^{-1}) = 45.2 - 46.7$. In this section we compare them with results and scaling relations present in the literature. Given that some assumptions are needed to compute outflow properties for both our AGNi and those in the literature, we try to mitigate the sys-

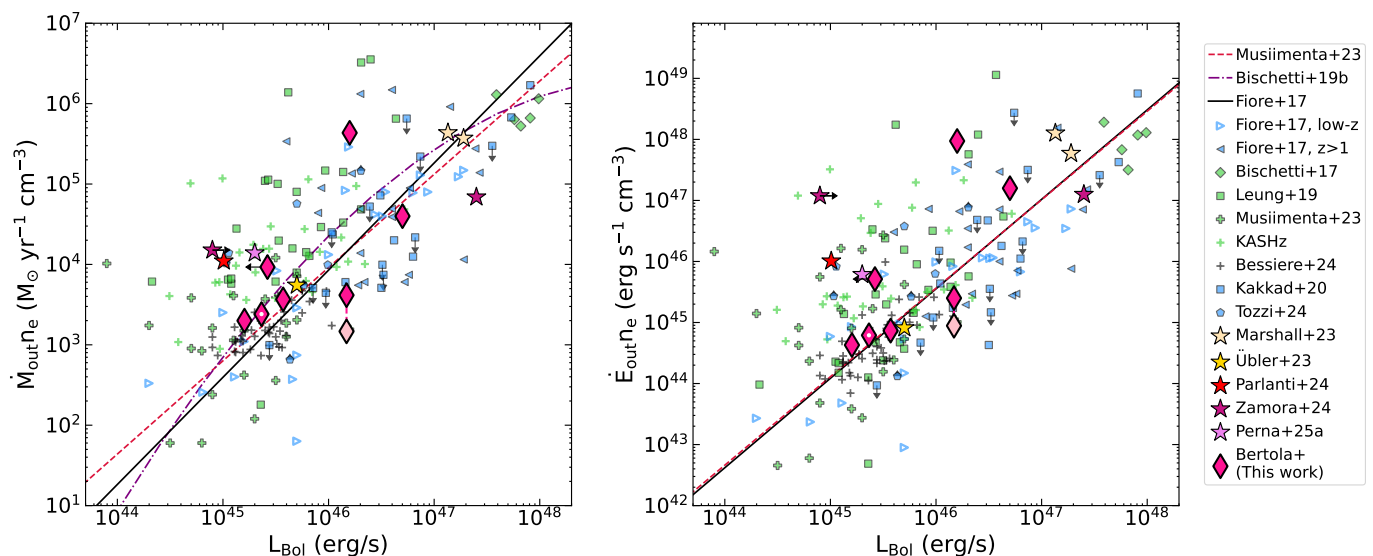


Fig. 6: Comparison of outflow properties of GA-NIFS COS-AGNi and literature samples in units of gas density. *Left*: Mass outflow rate against AGN bolometric luminosity. *Right*: Kinetic power as a function of AGN bolometric luminosity. The color coding of the single measurements is as in Fig. 1. Black solid lines mark the best-fit relation of Fiore et al. (2017), the purple dash-dotted line marks that from Bischetti et al. (2019b) and the red dashed lines mark the best fit relation of Masiimanta et al. (2023). We mark COS2949 with an additional white dot, being the only target at $z < 3.5$ in our sample. Pink diamonds show the outflow properties of COS349 as computed from the [O III] line and the magenta dashed line connects them with the estimates from the $H\alpha$ line.

tematics and limitations of such a comparison by recomputing literature measurements in a consistent way.

6.1. Close environment of COS-AGNi

JWST/NIRSpec IFU data showed that almost all the analyzed sources show clumps and/or reside in rich environments, a subset of which also present extended emission. Three of our COS-AGNi (COS2949, COS1118, COS590) are embedded in ionized gas extending on kpc scales that, given the typical sizes of galaxies at $z \approx 3.5$ ($r_e \approx 0.3$ kpc; e.g., Allen et al. 2017), reaches up to the circumgalactic medium. Four sources (COS2949, COS590, COS1638, COS1656) out of the six analyzed systems show companions, both as close-by AGNi (dual AGN: COS1638, COS1656), as galaxies (COS590; continuum is detected also at the location of the companions, see Fig. 2), and line-emitter clumps (COS2949). These could be tracing merging systems, given the close proximity of the companions and the ionized gas nebulae surrounding them. Moreover, the spatial distribution of the $H\alpha$ emission in COS2949 could be tracing the tidal tails produced by the close encounter of the AGN and (at least) one galaxy. However, we cannot investigate the relation between outflow strength and presence of companions or merger signatures due to the small size of the COS-AGNi sample. The [O III] nebula of COS1118 could resemble those observed in lower- z (and high- L_{bol}) AGNi by Liu et al. (2013a,b). However, given the observed kinematics (see Fig. A.4) and that the nebula is seen only in its [O III] emission, the present data offer no means to link it to the observed outflow.

6.2. Homogenization of outflow measurements

Given that the mass outflow rate and the kinetic power depend on the 1st- and 2nd-power of the outflow velocity, respectively, one of the main discriminant choice for a consistent recomputa-

tion of these outflow properties relies in the adopted definition of the outflow velocity, along with the availability of the outflow luminosity. The non-parametric fitting approach is very useful in determining phenomenological outflow properties (e.g., Harrison et al. 2016; Temple et al. 2019), yet it is not trivial to build a coherent literature sample because of the various line percentiles (2nd, 5th, 10th) at which the outflow velocity is measured at in the different works (e.g., Perrotta et al. 2019; Coatman et al. 2019). We adopt here the definition of outflow velocity as v_{max} (see Sect. 5.3.3), following Rupke & Veilleux (2013), which allows for a larger sample of literature results to be included compared to percentile velocities. For GA-NIFS COS-AGNi, the median v_{max} is approximately $1.2\times$ larger than the median $v_{\text{out}} = \max(v_{10}, v_{90})$ in our sample, leading to mass outflow rates and kinetic powers that are approximately $1.5\times$ and $1.9\times$ larger, respectively, than those computed with $v_{\text{out}} = \max(v_{10}, v_{90})$.

Another debated parameter is the outflow radial extent. In our comparison, we assume as outflow extent the maximum extent of the outflow relative to the source position, as defined in Sect. 5.3.3, that is, R_{max} . We compared the impact of different definitions of such parameters in our COS-AGNi. We find that R_{max} are roughly 2–3 times larger than flux-weighted radii.

Another key parameter in the outflow mass and energy budget computation is the gas electron density. This is one of the most difficult parameters to measure and is often assumed based on previous results, as also done in the present work. The determination of the best representative value of an outflow gas density is still currently widely debated in the literature. In fact, the outflow gas densities that can be found in the literature span at least one order of magnitude (from hundreds to thousands of cm^{-3} , Mingozzi et al. 2019; Förster Schreiber et al. 2019; Davies et al. 2020a; Speranza et al. 2024). Moreover, there is indication that the density of the perturbed gas in a single object can vary from a factor 3 up to more than one order of magnitude, as recently seen in XID2028 (Cresci et al. 2023) and the Teacup galaxy (Venturi et al. 2023), respectively. To overcome this limi-

tation, we compare outflow properties as a function of n_e , that is, we multiply each outflow parameter (mass outflow rate, kinetic power) by its outflow density as reported in the corresponding literature study. This approach is equivalent to assuming a gas density common to each outflow, as done for instance by [Fiore et al. \(2017\)](#) and [Musiimenta et al. \(2023\)](#), without selecting a representative value of the outflow density.

The parameter that most clearly affects the determination of the outflow mass, and thus also the mass outflow rate and kinetic power, is the gas density (e.g., [Harrison et al. 2018](#)). In fact, assuming a gas density of 200 cm^{-3} , as done for the scaling relations of [Fiore et al. \(2017\)](#) and [Musiimenta et al. \(2023\)](#), instead of 1000 cm^{-3} , as measured by [Förster Schreiber et al. \(2019\)](#) in the KMOS^{3D} stack, increases the outflow properties by a factor of five.

6.3. Literature measurements

Out of all the works listed in Sect. 2, we include in our comparison sample single measurements from the compilation in [Fiore et al. \(2017\)](#), from [Bessiere et al. \(2024\)](#), [Bischetti et al. \(2017\)](#), [Leung et al. \(2019\)](#), [Kakkad et al. \(2020\)](#), [Musiimenta et al. \(2023\)](#), and [Tozzi et al. \(2024\)](#), as well as from previous GA-NIFS works ([Marshall et al. 2023](#); [Übler et al. 2023](#); [Parlanti et al. 2024](#); [Zamora et al. 2024](#); [Perna et al. 2025a](#)). For all the listed works, if needed, we recomputed the outflow properties as $\dot{M}_{\text{out}} n_e$ and $E_{\text{out}} n_e$, using Eq. 4 with outflow parameters as described above. Results of [Bessiere et al. \(2024\)](#) were included scaling their measurements of v_{05} to v_{max} based on the v_{max} versus v_{05} relation measured for COS-AGNi ($\log(v_{\text{max}}/(1000 \text{ km/s})) = 0.12 + 0.81(\log(v_{05}/1000 \text{ km/s}))$). The results collected in [Fiore et al. \(2017\)](#) come both from slit spectroscopy and from spatially resolved data collected with ground-based telescopes. Regarding the results from slit spectroscopy, it is not possible to measure the outflow extent and so different works have made different assumptions. For instance, [Bischetti et al. \(2017\)](#) assume $R_{\text{max}} = 7 \text{ kpc}$ based on the analysis of the 2D spectra and [Leung et al. \(2019\)](#) build the radial profile of the outflows in the 2D spectra and measure its extent as the distance at which the outflow emission flux is 1/10 the strength of the maximum ($R_{\text{max}} = 0.3 - 11 \text{ kpc}$), while [Musiimenta et al. \(2023\)](#) assume as outflow extent for their $0.5 < z < 1$ eROSITA AGNi the effective radius of the host galaxies ($R_{\text{max}} = 2 - 10 \text{ kpc}$), that is the galaxy half-light radius as estimated from AGN-host galaxy image decomposition. Lastly, [Bessiere et al. \(2024\)](#) assume as outflow radius the mean deprojected outflow size measured in [Fischer et al. \(2018\)](#) from a combination of HST narrow-band imaging and STIS long-slit spectroscopy. Regarding the results from ground-based IFS, the AGNi of [Harrison et al. \(2012\)](#) and [Carniani et al. \(2015\)](#) were observed with SINFONI/VLT, as were SUPER AGNi ([Kakkad et al. 2020](#); [Tozzi et al. 2024](#)) but in adaptive-optics assisted mode, resulting in better spatial resolution. While [Carniani et al.](#) estimate the outflow radius from spectroastrometry analysis, [Harrison et al. \(2012\)](#) and [Tozzi et al.](#) use R_{max} , the latter additionally correcting for the PSF, and [Kakkad et al. \(2020\)](#) assume $R = 1 \text{ kpc}$ for all targets. We note that the differences between R_{max} and the flux-weighted radii for our GA-NIFS targets are approximately within a factor 2–3 \times , while radii in [Carniani et al.](#) and [Kakkad et al.](#) are roughly 5–7 \times smaller than the R_{max} of the rest of the compilation in [Fiore et al. \(2017\)](#). The choice of [Kakkad et al. \(2020\)](#) was driven by the fact that most of the SUPER Type 1 AGNi studied in their work show outflows that are unresolved compared to the PSF size. With the aim of best estimating the maximum outflow radii, we recompute

their mass outflow rates using the PSF size for the unresolved targets and D_{600} , that is the maximum projected spatial extent when considering the [O III] emission at $w_{80} > 600 \text{ km s}^{-1}$, for resolved targets. Lastly, we include KASHz AGNi ([Harrison et al. 2016](#)) using the updated fitting results that will be presented in [Scholtz et al. \(in prep\)](#). KASHz AGNi are typically unresolved because observed in seeing-limited conditions. Based on the results in [Scholtz et al. \(2020\)](#), we assumed $R_{\text{max}} = 3 \text{ kpc}$ as maximum outflow extent, which roughly corresponds to a median PSF of the KMOS observations presented in [Scholtz et al. \(2020\)](#).

Part of the outflows we collected from the literature are traced in the [O III] emission line. Following the calibration of [Fiore et al. \(2017\)](#), we rescale these measurements by assuming that the true outflow mass is 3 \times that measured using [O III] as tracer. Moreover, in the works of SUPER ([Kakkad et al. 2020](#); [Tozzi et al. 2024](#)), the authors measure the flux of the outflow from the wings of the multi-Gaussian line profiles ($|v| > 300 \text{ km s}^{-1}$), while we consider the full line profile of the broad components. [Kakkad et al.](#) and [Tozzi et al.](#) compared the two methods for SUPER Type 1 and Type 2 AGNi and report a difference of a factor 2 \times , which we use to rescale their results.

Lastly, we also include other recent results from the GA-NIFS GTO program by [Marshall et al. \(2023\)](#), [Übler et al. \(2023\)](#), [Parlanti et al. \(2024\)](#), [Perna et al. \(2025a\)](#) and [Zamora et al. \(2024\)](#), recomputing the outflow parameters if needed to align them to the assumptions used in this work.

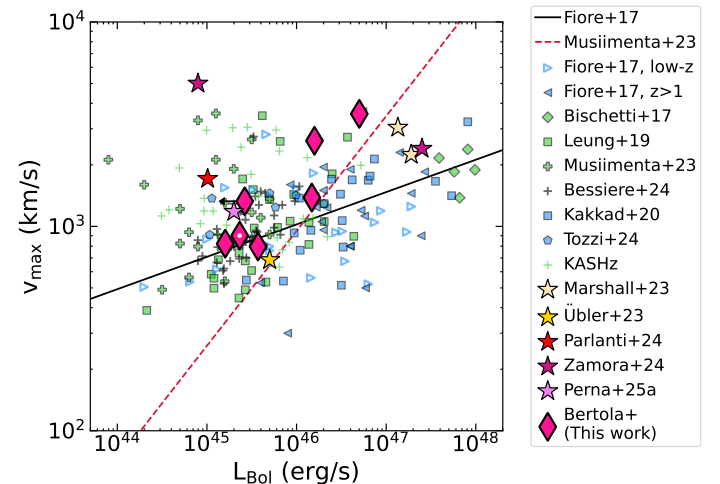


Fig. 7: Outflow velocity v_{max} as a function of bolometric luminosity of GA-NIFS COS-AGNi and literature samples used in this work. The color coding is the same as Fig. 1. The solid line marks the best fit relation of [Fiore et al. \(2017\)](#) and the dash-dotted line the best fit relation of [Musiimenta et al. \(2023\)](#).

6.4. Comparison with the literature

We show mass outflow rate and kinetic power against bolometric luminosity in Fig. 6, and outflow maximum velocity v_{max} against bolometric luminosity in Fig. 7. We report the \dot{M}_{out} versus L_{bol} , \dot{E}_{out} versus L_{bol} and the inverted L_{bol} versus v_{max} scaling relations of [Fiore et al. \(2017\)](#), that were built using the shown literature compilation homogenized in gas density, outflow radius and outflow geometry. We also show the more recent scaling relations of [Musiimenta et al. \(2023\)](#), which only considered AGNi beyond the local Universe ($z > 0.5$). The latter relations were obtained

for outflows of eROSITA AGNi and literature measurements homogenized in all parameters but the outflow velocity. Moreover, as mentioned in Sect. 6.3, Musiimenta et al. (2023) assume the effective radius of the host galaxies as outflow extent for their eROSITA AGNi. The main difference between Musiimenta et al. (2023) and Fiore et al. (2017) relations is a steeper v_{\max} versus L_{bol} relation of the former compared to that of the latter. We include the \dot{M}_{out} versus L_{bol} relation derived by Bischetti et al. (2019a), which predicts a flattening in the growth of the mass outflow rate in very bright sources ($\log(L_{\text{bol}}/\text{erg s}^{-1}) > 47$). All the shown scaling relations were scaled in gas density as done for the single measurements.

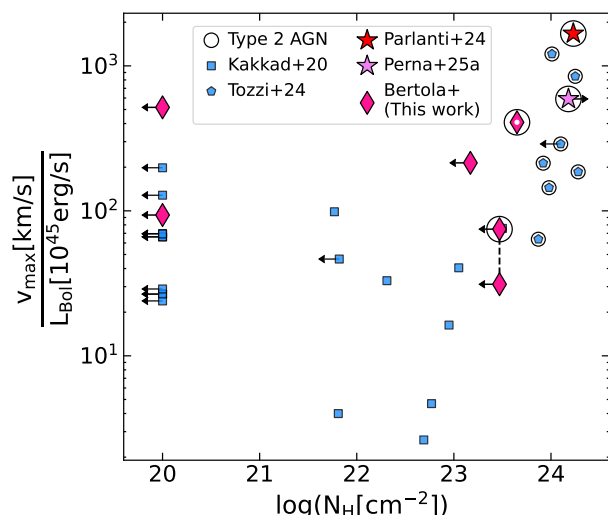


Fig. 8: Outflow maximum velocity normalized by the bolometric luminosity (in units of $10^{45} \text{ erg s}^{-1}$) versus column density adapted from Tozzi et al. (2024). The color coding and references are as in Fig. 1. Type 2 AGNi are marked with a black circle. COS1638-A (Type 1) and COS1638-B (Type 2) are connected by a dashed black line since the bolometric luminosity for this dual AGN was obtained from X-ray data integrated over the two components. COS2949, the only COS-AGNi at $z \approx 2$ and for which N_{H} is constrained, confirming its high-obscuration, is marked with an additional white dot. We note that SUPER AGNi (Kakkad et al. 2020; Tozzi et al. 2024) cover the redshift range $z = 2 - 2.6$ and GA-NIFS AGNi (except COS2949) span the $z = 3.5 - 4.8$ range (from Parlanti et al. 2024, Perna et al. 2025a and this work).

The outflows observed in $z \sim 3.5$ COS-AGNi and in other GA-NIFS AGNi previously analyzed (Marshall et al. 2023; Übler et al. 2023; Parlanti et al. 2024; Zamora et al. 2024; Perna et al. 2025a) span a range of \dot{M}_{out} and \dot{E}_{out} similar to that of literature measurements and are roughly consistent with the scaling relations in the \dot{M}_{out} versus L_{bol} plane. We note that roughly half of the GA-NIFS AGNi shown in Figs. 6-7 show energetics (\dot{M}_{out} , \dot{E}_{out}) larger than those predicted by the scaling relations of Fiore et al. (2017), Bischetti et al. (2019b) and Musiimenta et al. (2023). Given the strong fitting degeneracy between the BLR and the NLR components in COS349, we show its outflow properties as measured through both H α and [O III] (see Sect. 5.3.3), the latter corrected by a factor of 3 as done for the literature outflows traced in the [O III] line. The two measurements for COS349 are fairly in agreement with each other and consistent with the scatter of the literature measurements (see Fig. 6). There are two objects from GA-NIFS that are well above

the predictions, especially for what concerns the \dot{E}_{out} versus L_{bol} plane. These are COS1638-B from this work and the AGN-host submillimeter galaxy companion of the QSO BR1202-0725 (Zamora et al. 2024). Both targets show [O III] profiles that are totally dominated by the outflowing gas and could be identified as “blue-outliers” (e.g., Zamanov et al. 2002; Marziani et al. 2003; Cracco et al. 2016; Perna et al. 2021; Lanzuisi et al. 2024). GA-NIFS COS-AGNi are also well consistent with the parameter space spanned by literature AGNi in the v_{\max} vs L_{bol} plane, with a general tendency to lie at faster velocities than those predicted by the relations of Fiore et al. (2017) and Musiimenta et al. (2023). Given the uncharted $z - L_{\text{bol}}$ parameter space covered by COS-AGNi, this result indicates no significant evolution of the physics driving outflows beyond $z \approx 3$.

We note that GA-NIFS COS-AGNi are the only non-extreme AGNi at $z > 3$ that were studied so far for their outflow properties. In fact, even though only the results for WISSH AGNi allowed us to compute the outflow energetics following the approach of Fiore et al. (2017), only observations of extremely bright AGNi ($\log(L_{\text{bol}}/\text{erg s}^{-1}) > 46.7$) have been able to probe AGN-driven outflows, due to sensitivity limitations and lower S/N even in spatially integrated spectra. We note that Suh et al. (2025) recently presented JWST/NIRSpec IFU data of a low-mass AGN at $z \lesssim 4$ that is accreting at super-Eddington rates and shows prominent outflows, whose properties were computed using assumptions that cannot be homogenized to ours.

Outflows detected in COS-AGNi are less extended than what assumed in literature works using unresolved slit spectroscopy, especially at these redshifts (e.g., $R_{\text{max}} \approx 7 \text{ kpc}$, Bischetti et al. 2017). These are equal to twice the maximum radii ($\langle R_{\text{max}} \rangle \approx 2.5 \text{ kpc}$) and seven times the flux-weighted radii ($\langle R_{\text{max}} \rangle \approx 1 \text{ kpc}$) of COS-AGNi, while the radii reported in Shen (2016) can be even larger ($R \approx 5 - 15 \text{ kpc}$)⁸. There is also indication that Extremely-Red Quasars (ERQs) show more compact (by roughly a factor 2 \times) and faster outflows (by roughly a factor 3 \times) compared to blue AGNi (Perrotta et al. 2019; Lau et al. 2024), and that Type 2 AGNi show more extended outflows compared to Type 1 AGNi (Tozzi et al. 2024). Moreover, Tozzi et al. (2024) showed that Compton-Thick AGNi (i.e., highly obscured, $\log N_{\text{H}} > 24$, in the X-rays) harbor faster outflows compared to their Type 1 and less-obscured counterparts matched in AGN bolometric luminosity, suggesting a relevant role of radiation pressure on dust in outflow acceleration. The findings of Perrotta et al., Lau et al. and Tozzi et al. can be interpreted in terms of the evolutionary scenario from obscured accretion to shining AGNi through the “blow-out” phase (e.g., Lapi et al. 2014) at different AGN power.

We show in Fig. 8 the distribution of SUPER and GA-NIFS AGNi in terms of maximum outflow velocity over bolometric luminosity as a function of nuclear column density. Figure 8 shows that GA-NIFS AGNi at $z > 3$ presented in previous studies (Parlanti et al. 2024; Perna et al. 2025a) and in this work (see Tables 1 and 2) tentatively follow the “faster outflows in highly obscured AGNi” trend seen by Tozzi et al. (2024) for AGNi at $z = 2 - 2.5$. The Kolmogorov-Smirnov test applied to Type 1 versus Type 2 AGNi in GANIFS (or in the COS-AGNi sample only) is inconclusive, due to the very small sample size. A larger sample of AGNi would be needed to confirm this behavior at $z > 2.5$. We note that the bolometric luminosity estimated from SED fit-

⁸ We note that these values are mentioned in the main text of Shen (2016) but are not tabulated in the provided catalog. We thus chose not to include outflow measurements from this work in our comparison given the absence of such an info target by target.

ting for COS1118 (highest v_{\max}/L_{bol} for $\log N_{\text{H}} < 20$) might not be well constrained due to a poor photometric coverage of the target, mainly dominated by upper limits in the IR regime, leading to an overestimated v_{\max}/L_{bol} in Fig. 8. In fact, using the relations derived by Duras et al. (2020), we find an X-ray-based bolometric luminosity $\log(L_{\text{bol}}/\text{erg s}^{-1}) = 45.6$, that is ≈ 0.5 dex larger than that obtained from SED fitting (see Table 1), which would move COS1118 closer to the other Type 1 AGNi with no obscuration in the X-rays.

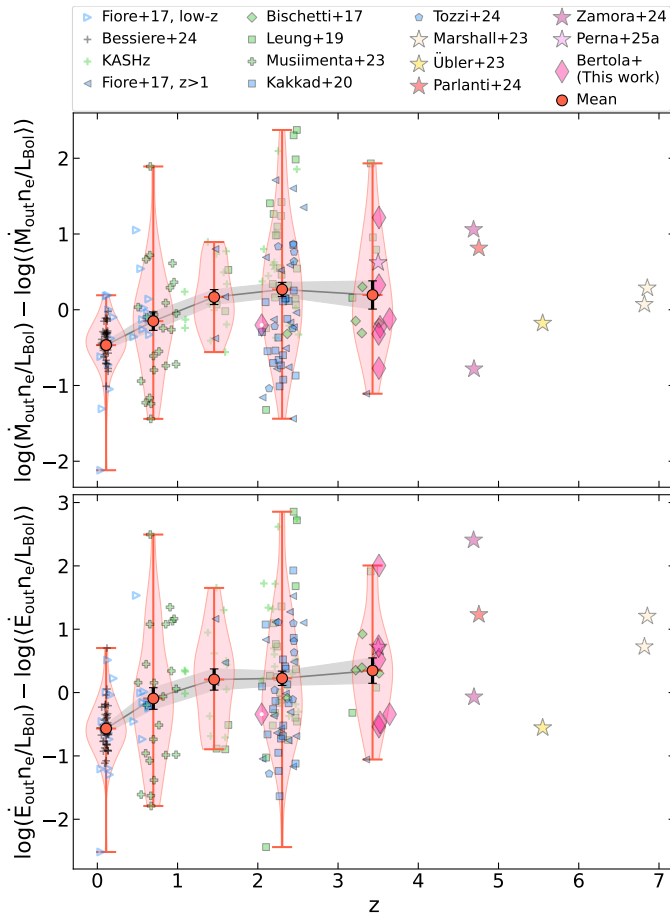


Fig. 9: Ratio of mass outflow rate times gas density over bolometric luminosity (top) and ratio of kinetic power times gas density over bolometric luminosity (bottom), normalized to their sample means, versus redshift. Samples and color coding are the same as Fig. 6. Violin plots show the distribution in each considered redshift bin, red circles mark the mean of each redshift bin and black vertical error bars mark the standard deviation of the mean. Points at $z > 4$ are shown to highlight the few measurements available. We note that only other two AGNi at $z > 4$ were observed by JWST (Loiacono et al. 2024; Suh et al. 2025) and are not part of the plot due to the impossibility of homogenizing their measurements with our assumptions in Sect. 6.2.

Lastly, we investigate the possibility of a redshift evolution of the strength of outflows up to redshift $z = 4$, where measurements become too sparse. Figure 9 shows the redshift evolution of the logarithm of the ratio of $M_{\text{out}}n_e$ (left), that is the mass outflow rate for a parameterized gas density, and of $E_{\text{out}}n_e$ (right), that is the outflow kinetic power for a parameterized gas density, over AGN bolometric luminosity L_{bol} , normalized at their mean values computed across all redshifts. We divide the col-

lected measurements in five redshift bins ($0.08 < z < 0.45$, $0.45 \leq z < 1$, $1 \leq z < 2$, $2 \leq z < 3$, $3 \leq z < 4$) and compute the mean $M_{\text{out}}n_e/L_{\text{bol}}$ in each bin. While the scatter is large, as the violin plots indicate, the mean values do not show any evidence of evolution beyond $z > 1$. We note that repeating this exercise for the mass outflow rate and the bolometric luminosity separately returns an increasing trend of the mean values for increasing redshift. Outflows at $z \approx 0$ in Fig. 9 appear to be less energetic than those at $z > 1$ by more than one, but less than two, standard deviations. This behavior holds also when excluding the outlier at lower $M_{\text{out}}(E_{\text{out}})$ in the $z \approx 0$ bin and the outlier at larger $M_{\text{out}}(E_{\text{out}})$ in the $z \approx 0.5$ bin. However, we caution that there are many other works at $z < 0.5$ that could not be included because the reported measurements could not be homogenized with our assumptions. We also caution that there are many caveats in the results shown Fig. 9, the main one being that the collected measurements allow for a rather sparse or non-exhaustive sampling of some redshift bins, like the at $z \approx 1.5$ and at $0.08 < z < 0.45$, respectively. Moreover, having parameterized the outflow gas density, the comparison as is in Fig. 9 is equal to assuming that each outflow has the same gas density.

Maiolino et al. (2025) recently investigated the *Chandra*-JWST properties of AGNi selected based on the presence of the BLR. They find that the majority of such JWST-selected AGNi at $z > 4$ do not show evidence of prominent outflows, and claim it is in contrast with lower redshift or higher luminosity, at odds with our result of no redshift evolution. One possible explanation is that COS-AGNi are a sample of X-ray selected AGNi and the majority of the literature AGNi are X-ray detected, while the bulk of JWST-selected AGN are X-ray undetected, as also remarked by Maiolino et al.. This could support the scenario in which the X-ray weakness of JWST-selected AGNi could be due to weaker outflows (possibly because of lower metallicity, which is the key factor in driving both nuclear-line locking- and extended -dust driven- outflows). Hence, more gas would linger around the BH in these JWST-selected AGNi, causing large covering factor of Compton thick material which makes them X-ray weak. The AGNi that are X-ray selected (or X-ray detected) are instead those in which the outflow managed to develop and clear some of the nuclear gas to make X-rays easier to detect, possibly because such X-ray detected AGNi are more metal rich or because they are more evolved, giving radiation pressure more time to interact with the ISM.

7. Summary and conclusions

We have presented the analysis of JWST/NIRSpec IFU data from the GA-NIFS GTO program of seven $z \approx 3.5$ AGNi with $45.2 < \log(L_{\text{bol}}/\text{erg s}^{-1}) < 46.7$ (two of which are part of a dual-AGN system; Perna et al. 2025b) that were selected in X-rays ($\log(L_{\text{X}}/\text{erg s}^{-1}) > 44$) from the COSMOS-Legacy field (Marchesi et al. 2016). The capabilities of JWST/NIRSpec IFU allowed an uncharted $L_{\text{bol}} - z$ parameter space to be probed, as highlighted in Fig. 1. In fact, we have sampled for the first time the rest-frame optical properties of a sample of AGNi at $z \approx 3.5$ and $\log(L_{\text{bol}}/\text{erg s}^{-1}) = 45.2 - 46.7$, collecting spectra of a high S/N and broad wavelength range and with the added benefit of the spatially resolved information provided by IFU data.

- We investigated the ionized gas properties of our AGNi both in a spaxel-by-spaxel fitting approach and from integrated spectra, with the main aim of studying their outflows. Outflow properties were derived from spectra integrated over the “outflow region,” identified as the 3σ emission region

of the H α or [O III] broad component maps (or H α or [N II] broad component maps for COS2949) based on whichever was most extended.

- We find that the majority of our targets show close-by companions and clumps, both in the form of galaxies (COS590, COS2949) and dual AGNi systems (COS1656, COS1638; see also Perna et al. 2025b). Moreover, a good fraction of the objects are embedded in diffused ionized emission characterized by low-velocity dispersion and moderate-velocity displacement with respect to the AGNi rest frame (COS1638, COS590, COS2949, COS1118) and with kinematics that appear to be unrelated to the outflows, which are mostly confined to the proximity of the AGN.
- We derived the outflow properties of our targets and compared our results with those present in the literature, both from slit spectroscopy and IFS data (see Fig. 6–7). We homogenized the literature measurements to those of Fiore et al. (2017) and Musiimenta et al. (2023) for a consistent comparison with their scaling relations. Given the very different results and assumptions that are present in the literature regarding the outflow gas electron density, we scaled the outflow properties by the outflow gas density to obtain a comparison that is not dependent on the outflow gas density.
- We find that outflows observed in COS-AGNi are well consistent with the previous results in the \dot{M}_{out} versus L_{bol} , \dot{E}_{out} versus L_{bol} , and v_{max} versus L_{bol} parameter spaces and that they mostly fall close to or above previous scaling relations (e.g., Fiore et al. 2017; Bischetti et al. 2019a; Musiimenta et al. 2023).
- The GA-NIFS AGNi (COS-AGNi complemented with GA-NIFS AGNi from the literature; Übler et al. 2023; Parlanti et al. 2024; Perna et al. 2025a) tentatively follow the trend discovered by Tozzi et al. (2024) in AGNi at $z \approx 2 - 2.5$, that is, showing faster outflows for the thickest absorbers as traced in the X-rays, while we find no clear redshift evolution of $\dot{M}_{\text{out}} n_e / L_{\text{bol}}$ and $\dot{E}_{\text{out}} n_e / L_{\text{bol}}$ beyond $z > 1$ (Fig. 9).
- In general, the trends shown by GA-NIFS AGNi at $z > 3$ are similar to those observed at lower redshifts, suggesting that the nature of AGN feedback does not significantly evolve beyond $z \approx 3$.

The unprecedented capabilities of JWST have opened a new window in extragalactic astrophysics, enabling for the first time to characterize the ionized gas properties as traced by optical emission lines like H α and [O III] in high- z galaxies up to cosmic dawn. In the field of AGN feedback and AGN/galaxy co-evolution, future observations with JWST/NIRSpec will provide statistical samples provide statistical samples of AGN at $z > 4$ to assess the properties and effects of AGN-driven ionized outflows in the key phase of galaxy evolution, that is the cosmic epoch between cosmic noon and cosmic dawn.

Acknowledgements. EB and GC acknowledge financial support from INAF under the Large Grant 2022 “The metal circle: a new sharp view of the baryon cycle up to Cosmic Dawn with the latest generation IFU facilities”. EB acknowledges financial support from INAF through the “Ricerca Fondamentale 2024” program (mini-grant 1.05.24.07.01). AJB acknowledges funding from the “FirstGalaxies” Advanced Grant from the European Research Council (ERC) under the European Union’s Horizon 2020 research and innovation program (Grant agreement No. 789056). HÜ acknowledges funding by the European Union (ERC APEX, 101164796). Views and opinions expressed are however those of the authors only and do not necessarily reflect those of the European Union or the European Research Council Executive Agency. Neither the European Union nor the granting authority can be held responsible for them. RM acknowledges support by the Science and Technology Facilities Council (STFC), from the ERC Advanced Grant 695671 “QUENCH”, and funding from a research professorship from the Royal Society. JS acknowledges support by the

Science and Technology Facilities Council (STFC), by the ERC through Advanced Grant 695671 “QUENCH”, and by the UKRI Frontier Research grant RISEandFALL. MP, SA, and BRdP acknowledge grant PID2021-127718NB-I00 funded by the Spanish Ministry of Science and Innovation/State Agency of Research (MICIN/AEI/10.13039/501100011033). MP also acknowledges the grant RYC2023-044853-I, funded by MICIU/AEI/10.13039/501100011033 and European Social Fund Plus (FSE+). IL acknowledges support from PRIN-MUR project “PROMETEUS” financed by the European Union - Next Generation EU, Mission 4 Component 1 CUP B53D23004750006. SC and GV acknowledge support from the European Union (ERC, WINGS,101040227). G.T. acknowledges financial support from the European Research Council (ERC) Advanced Grant under the European Union’s Horizon Europe research and innovation programme (grant agreement AdG GALPHYS, No. 101055023).

References

- Alexander, D. M., Swinbank, A. M., Smail, I., McDermid, R., & Nesvadba, N. P. H. 2010, *MNRAS*, 402, 2211
- Allen, R. J., Kacprzak, G. G., Glazebrook, K., et al. 2017, *ApJ*, 834, L11
- Baldwin, J. A., Phillips, M. M., & Terlevich, R. 1981, *PASP*, 93, 5
- Barbary, K. 2016, extinction v0.3.0
- Baron, D. & Netzer, H. 2019, *MNRAS*, 486, 4290
- Bessiere, P. S., Ramos Almeida, C., Holden, L. R., Tadhunter, C. N., & Canalizo, G. 2024, *A&A*, 689, A271
- Bischetti, M., Feruglio, C., D’Odorico, V., et al. 2022, *Nature*, 605, 244
- Bischetti, M., Maiolino, R., Carniani, S., et al. 2019a, *A&A*, 630, A59
- Bischetti, M., Piconcelli, E., Feruglio, C., et al. 2019b, *A&A*, 628, A118
- Bischetti, M., Piconcelli, E., Vietri, G., et al. 2017, *A&A*, 598, A122
- Böker, T., Arribas, S., Lützgendorf, N., et al. 2022, *A&A*, 661, A82
- Boquien, M., Burgarella, D., Roehlly, Y., et al. 2019, *A&A*, 622, A103
- Brusa, M., Bongiorno, A., Cresci, G., et al. 2015, *MNRAS*, 446, 2394
- Brusa, M., Comastri, A., Gilli, R., et al. 2009, *ApJ*, 693, 8
- Brusa, M., Cresci, G., Daddi, E., et al. 2018, *A&A*, 612, A29
- Brusa, M., Perna, M., Cresci, G., et al. 2016, *A&A*, 588, A58
- Caglar, T., Koss, M. J., Bartscher, L., et al. 2023, *ApJ*, 956, 60
- Cano-Díaz, M., Maiolino, R., Marconi, A., et al. 2012, *A&A*, 537, L8
- Cappellari, M. 2023, *MNRAS*, 526, 3273
- Cappellari, M. & Emsellem, E. 2004, *PASP*, 116, 138
- Cappi, M., Panessa, F., Bassani, L., et al. 2006, *A&A*, 446, 459
- Cardelli, J. A., Clayton, G. C., & Mathis, J. S. 1989, *ApJ*, 345, 245
- Carnall, A. C., McLure, R. J., Dunlop, J. S., et al. 2023, *Nature*, 619, 716
- Carniani, S., Marconi, A., Maiolino, R., et al. 2015, *A&A*, 580, A102
- Carniani, S., Marconi, A., Maiolino, R., et al. 2016, *A&A*, 591, A28
- Carniani, S., Marconi, A., Maiolino, R., et al. 2017, *A&A*, 605, A105
- Chabrier, G. 2003, *ApJ*, 586, L133
- Chartas, G., Cappi, M., Vignali, C., et al. 2021, *ApJ*, 920, 24
- Chisholm, J., Berg, D. A., Endsley, R., et al. 2024, *MNRAS*, 534, 2633
- Cicone, C., Brusa, M., Ramos Almeida, C., et al. 2018, *Nature Astronomy*, 2, 176
- Cicone, C., Maiolino, R., Gallerani, S., et al. 2015, *A&A*, 574, A14
- Cicone, C., Maiolino, R., Sturm, E., et al. 2014, *A&A*, 562, A21
- Circosta, C., Mainieri, V., Padovani, P., et al. 2018, *A&A*, 620, A82
- Coatman, L., Hewett, P. C., Banerji, M., et al. 2019, *MNRAS*, 486, 5335
- Costa, T., Pakmor, R., & Springel, V. 2020, *MNRAS*, 497, 5229
- Costa, T., Rosdahl, J., Sijacki, D., & Haehnelt, M. G. 2018, *MNRAS*, 479, 2079
- Cracco, V., Ciroi, S., Berton, M., et al. 2016, *MNRAS*, 462, 1256
- Cresci, G., Mainieri, V., Brusa, M., et al. 2015a, *ApJ*, 799, 82
- Cresci, G. & Maiolino, R. 2018, *Nature Astronomy*, 2, 179
- Cresci, G., Marconi, A., Zibetti, S., et al. 2015b, *A&A*, 582, A63
- Cresci, G., Tozzi, G., Perna, M., et al. 2023, *A&A*, 672, A128
- Cresci, G., Vanzì, L., Telles, E., et al. 2017, *A&A*, 604, A101
- Davies, R., Baron, D., Shimizu, T., et al. 2020a, *MNRAS*, 498, 4150
- Davies, R. L., Förster Schreiber, N. M., Lutz, D., et al. 2020b, *ApJ*, 894, 28
- D’Eugenio, F., Pérez-González, P. G., Maiolino, R., et al. 2024, *Nature Astronomy*, 8, 1443
- Di Matteo, T., Springel, V., & Hernquist, L. 2005, *Nature*, 433, 604
- Duras, F., Bongiorno, A., Piconcelli, E., et al. 2017, *A&A*, 604, A67
- Duras, F., Bongiorno, A., Ricci, F., et al. 2020, *A&A*, 636, A73
- Feruglio, C., Ferrara, A., Bischetti, M., et al. 2017, *A&A*, 608, A30
- Fiore, F., Feruglio, C., Shankar, F., et al. 2017, *A&A*, 601, A143
- Fischer, T. C., Kraemer, S. B., Schmitt, H. R., et al. 2018, *ApJ*, 856, 102
- Fluetsch, A., Maiolino, R., Carniani, S., et al. 2019, *MNRAS*, 483, 4586
- Förster Schreiber, N. M., Übler, H., Davies, R. L., et al. 2019, *ApJ*, 875, 21
- Förster Schreiber, N. M. & Wuyts, S. 2020, *ARA&A*, 58, 661
- Furtak, L. J., Labbé, I., Zitron, A., et al. 2024, *Nature*, 628, 57
- Gallagher, R., Maiolino, R., Belfiore, F., et al. 2019, *MNRAS*, 485, 3409
- Gardner, J. P., Mather, J. C., Abbott, R., et al. 2023, *PASP*, 135, 068001
- Genzel, R., Förster Schreiber, N. M., Rosario, D., et al. 2014, *ApJ*, 796, 7

- Greene, J. E., Labbe, I., Goulding, A. D., et al. 2024, *ApJ*, 964, 39
- Harikane, Y., Zhang, Y., Nakajima, K., et al. 2023, *ApJ*, 959, 39
- Harrison, C. M. 2017, *Nature Astronomy*, 1, 0165
- Harrison, C. M., Alexander, D. M., Mullaney, J. R., et al. 2016, *MNRAS*, 456, 1195
- Harrison, C. M., Alexander, D. M., Mullaney, J. R., & Swinbank, A. M. 2014, *MNRAS*, 441, 3306
- Harrison, C. M., Alexander, D. M., Swinbank, A. M., et al. 2012, *MNRAS*, 426, 1073
- Harrison, C. M., Costa, T., Tadhunter, C. N., et al. 2018, *Nature Astronomy*, 2, 198
- Harrison, C. M. & Ramos Almeida, C. 2024, *Galaxies*, 12, 17
- Hasinger, G., Capak, P., Salvato, M., et al. 2018, *ApJ*, 858, 77
- Hopkins, P. F. & Elvis, M. 2010, *MNRAS*, 401, 7
- Husemann, B., Davis, T. A., Jahnke, K., et al. 2017, *MNRAS*, 470, 1570
- Husemann, B., Jahnke, K., Sánchez, S. F., et al. 2014, *MNRAS*, 443, 755
- Husemann, B., Wisotzki, L., Sánchez, S. F., & Jahnke, K. 2013, *A&A*, 549, A43
- Igo, Z., Parker, M. L., Matzeu, G. A., et al. 2020, *MNRAS*, 493, 1088
- Isobe, Y., Ouchi, M., Nakajima, K., et al. 2023, *ApJ*, 956, 139
- Jakobsen, P., Ferruit, P., Alves de Oliveira, C., et al. 2022, *A&A*, 661, A80
- Kakkad, D., Mainieri, V., Vietri, G., et al. 2020, *A&A*, 642, A147
- Karouzos, M., Woo, J.-H., & Bae, H.-J. 2016, *ApJ*, 833, 171
- Kauffmann, G., Heckman, T. M., Tremonti, C., et al. 2003, *MNRAS*, 346, 1055
- Kewley, L. J., Dopita, M. A., Leitherer, C., et al. 2013, *ApJ*, 774, 100
- Kewley, L. J., Dopita, M. A., Sutherland, R. S., Heisler, C. A., & Trevena, J. 2001, *ApJ*, 556, 121
- Kewley, L. J., Groves, B., Kauffmann, G., & Heckman, T. 2006, *MNRAS*, 372, 961
- King, A. & Pounds, K. 2015, *ARA&A*, 53, 115
- Kocevski, D. D., Onoue, M., Inayoshi, K., et al. 2023, *ApJ*, 954, L4
- Kormendy, J. & Ho, L. C. 2013, *ARA&A*, 51, 511
- Kovačević, J., Popović, L. Č., & Dimitrijević, M. S. 2010, *ApJS*, 189, 15
- Laha, S., Reynolds, C. S., Reeves, J., et al. 2021, *Nature Astronomy*, 5, 13
- Lamperti, I., Arribas, S., Perna, M., et al. 2024, *A&A*, 691, A153
- Lanzuisi, G., Matzeu, G., Baldini, P., et al. 2024, *A&A*, 689, A247
- Lapi, A., Raimundo, S., Aversa, R., et al. 2014, *ApJ*, 782, 69
- Lau, M. W., Perrotta, S., Hamann, F., et al. 2024, *MNRAS*, 532, 2044
- Leung, G. C. K., Coil, A. L., Aird, J., et al. 2019, *ApJ*, 886, 11
- Li, S., Wang, X., Chen, Y., et al. 2024, *ApJ*, accepted
- Lilly, S. J., Le Fèvre, O., Renzini, A., et al. 2007, *ApJS*, 172, 70
- Liu, G., Zakamska, N. L., & Greene, J. E. 2014, *MNRAS*, 442, 1303
- Liu, G., Zakamska, N. L., Greene, J. E., Nesvadba, N. P. H., & Liu, X. 2013a, *MNRAS*, 430, 2327
- Liu, G., Zakamska, N. L., Greene, J. E., Nesvadba, N. P. H., & Liu, X. 2013b, *MNRAS*, 436, 2576
- Liu, W., Fan, X., Yang, J., et al. 2024, *ApJ*, 976, 33
- Loiacono, F., Decarli, R., Mignoli, M., et al. 2024, *A&A*, 685, A121
- Lutz, D., Sturm, E., Janssen, A., et al. 2020, *A&A*, 633, A134
- Madau, P. & Dickinson, M. 2014, *ARA&A*, 52, 415
- Magorrian, J., Tremaine, S., Richstone, D., et al. 1998, *AJ*, 115, 2285
- Maiolino, R., Gallerani, S., Neri, R., et al. 2012, *MNRAS*, 425, L66
- Maiolino, R., Risaliti, G., Signorini, M., et al. 2025, *MNRAS*, 538, 1921
- Maiolino, R., Scholtz, J., Witsok, J., et al. 2024, *Nature*, 627, 59
- Marasco, A., Cresci, G., Nardini, E., et al. 2020, *A&A*, 644, A15
- Marchesi, S., Lanzuisi, G., Civano, F., et al. 2016, *ApJ*, 830, 100
- Marconcin, C., D'Eugenio, F., Maiolino, R., et al. 2024, *MNRAS*, 533, 2488
- Marshall, M. A., Perna, M., Willott, C. J., et al. 2023, *A&A*, 678, A191
- Marshall, M. A., Yue, M., Eilers, A.-C., et al. 2024, s, submitted to *A&A*
- Marziani, P., Zamanov, R., Sulentic, J. W., Calvani, M., & Dultzin-Hacyan, D. 2003, *Mem. Soc. Astron. Italiana*, 74, 492
- Matzeu, G. A., Brusa, M., Lanzuisi, G., et al. 2023, *A&A*, 670, A182
- Mazzolari, G., Übler, H., Maiolino, R., et al. 2024, *A&A*, 691, A345
- McConnell, N. J., Ma, C.-P., Gebhardt, K., et al. 2011, *Nature*, 480, 215
- Mingozzi, M., Cresci, G., Venturi, G., et al. 2019, *A&A*, 622, A146
- Morganti, R., Veilleux, S., Oosterloo, T., Teng, S. H., & Rupke, D. 2016, *A&A*, 593, A30
- Musiimenta, B., Brusa, M., Liu, T., et al. 2023, *A&A*, 679, A84
- Nesvadba, N. P. H., Lehnert, M. D., De Breuck, C., Gilbert, A. M., & van Breugel, W. 2008, *A&A*, 491, 407
- Nesvadba, N. P. H., Lehnert, M. D., Eisenhauer, F., et al. 2006, *ApJ*, 650, 693
- Osterbrock, D. E. & Ferland, G. J. 2006, *Astrophysics of gaseous nebulae and active galactic nuclei*
- Pâris, I., Petitjean, P., Aubourg, É., et al. 2014, *A&A*, 563, A54
- Parlanti, E., Carniani, S., Übler, H., et al. 2024, *A&A*, 684, A24
- Perna, M., Arribas, S., Colina, L., et al. 2022, *A&A*, 662, A94
- Perna, M., Arribas, S., Ji, X., et al. 2025a, *A&A*, 694, A170
- Perna, M., Arribas, S., Lamperti, I., et al. 2025b, *A&A*, 696, A59
- Perna, M., Arribas, S., Marshall, M., et al. 2023, *A&A*, 679, A89
- Perna, M., Arribas, S., Pereira Santaella, M., et al. 2021, *A&A*, 646, A101
- Perna, M., Brusa, M., Cresci, G., et al. 2015a, *A&A*, 574, A82
- Perna, M., Brusa, M., Salvato, M., et al. 2015b, *A&A*, 583, A72
- Perna, M., Lanzuisi, G., Brusa, M., Mignoli, M., & Cresci, G. 2017, *A&A*, 603, A99
- Perrotta, S., Hamann, F., Zakamska, N. L., et al. 2019, *MNRAS*, 488, 4126
- Planck Collaboration, Aghanim, N., Akrami, Y., et al. 2020, *A&A*, 641, A6
- Puglisi, A., Daddi, E., Valentino, F., et al. 2021, *MNRAS*, 508, 5217
- Rodríguez Del Pino, B., Perna, M., Arribas, S., et al. 2024, *A&A*, 684, A187
- Rupke, D. S. N., Gültekin, K., & Veilleux, S. 2017, *ApJ*, 850, 40
- Rupke, D. S. N. & Veilleux, S. 2013, *ApJ*, 768, 75
- Saccheo, I., Bongiorno, A., Piconcelli, E., et al. 2023, *A&A*, 671, A34
- Sanders, R. L., Shapley, A. E., Topping, M. W., Reddy, N. A., & Brammer, G. B. 2023, *ApJ*, 955, 54
- Scholtz, J., Harrison, C. M., Rosario, D. J., et al. 2020, *MNRAS*, 492, 3194
- Scholtz, J., Maiolino, R., D'Eugenio, F., et al. 2023, s, arXiv:2311.18731
- Schreiber, C., Pannella, M., Elbaz, D., et al. 2015, *A&A*, 575, A74
- Shapley, A. E., Sanders, R. L., Topping, M. W., et al. 2025, *ApJ*, 980, 242
- Shen, Y. 2016, *ApJ*, 817, 55
- Speranza, G., Ramos Almeida, C., Acosta-Pulido, J. A., et al. 2024, *A&A*, 681, A63
- Strateva, I., Ivezić, Ž., Knapp, G. R., et al. 2001, *AJ*, 122, 1861
- Strom, A. L., Steidel, C. C., Rudie, G. C., et al. 2017, *ApJ*, 836, 164
- Suh, H., Scharwächter, J., Farina, E. P., et al. 2025, *Nature Astronomy*, 9, 271
- Temple, M. J., Banerji, M., Hewett, P. C., et al. 2019, *MNRAS*, 487, 2594
- Temple, M. J., Rankine, A. L., Banerji, M., et al. 2024, *MNRAS*, 532, 424
- Tozzi, G., Cresci, G., Marasco, A., et al. 2021, *A&A*, 648, A99
- Tozzi, G., Cresci, G., Perna, M., et al. 2024, *A&A*, 690, A141
- Trakhtenbrot, B., Civano, F., Urry, C. M., et al. 2016, *ApJ*, 825, 4
- Travascio, A., Piconcelli, E., Bischetti, M., et al. 2024, *A&A*, 686, A250
- Trump, J. R., Impey, C. D., Elvis, M., et al. 2009, *ApJ*, 696, 1195
- Übler, H., Maiolino, R., Curtis-Lake, E., et al. 2023, *A&A*, 677, A145
- Ulvri, L., Venturi, G., Cresci, G., et al. 2024, *A&A*, 685, A122
- van Dokkum, P. G. 2001, *PASP*, 113, 1420
- Vayner, A., Wright, S. A., Murray, N., et al. 2021a, *ApJ*, 919, 122
- Vayner, A., Zakamska, N. L., Ishikawa, Y., et al. 2024, *ApJ*, 960, 126
- Vayner, A., Zakamska, N. L., Riffel, R. A., et al. 2021b, *MNRAS*, 504, 4445
- Veilleux, S., Maiolino, R., Bolatto, A. D., & Aalto, S. 2020, *A&A Rev.*, 28, 2
- Veilleux, S. & Osterbrock, D. E. 1987, *ApJS*, 63, 295
- Venturi, G., Nardini, E., Marconi, A., et al. 2018, *A&A*, 619, A74
- Venturi, G., Treister, E., Finlez, C., et al. 2023, *A&A*, 678, A127
- Vietri, G., Mainieri, V., Kakkad, D., et al. 2020, *A&A*, 644, A175
- Vietri, G., Misawa, T., Piconcelli, E., et al. 2022, *A&A*, 668, A87
- Vietri, G., Piconcelli, E., Bischetti, M., et al. 2018, *A&A*, 617, A81
- Ward, S. R., Costa, T., Harrison, C. M., & Mainieri, V. 2024, *MNRAS*, 533, 1733
- Wylezalek, D., Zakamska, N. L., Liu, G., & Obied, G. 2016, *MNRAS*, 457, 745
- Yang, G., Boquien, M., Brandt, W. N., et al. 2022, *ApJ*, 927, 192
- Yang, G., Boquien, M., Buat, V., et al. 2020, *MNRAS*, 491, 740
- Yang, J., Wang, F., Fan, X., et al. 2021, *ApJ*, 923, 262
- Zakamska, N. L., Lampayan, K., Petric, A., et al. 2016, *MNRAS*, 455, 4191
- Zamanov, R., Marziani, P., Sulentic, J. W., et al. 2002, *ApJ*, 576, L9
- Zamora, S., Venturi, G., Carniani, S., et al. 2024, submitted to *A&A*
- Zanchettin, M. V., Feruglio, C., Massardi, M., et al. 2023, *A&A*, 679, A88

Appendix A: Maps and spectra

We present in this appendix the full spectra (Fig. A.1-A.3), the maps of total, narrow and broad [O III] emission line components plus the close-up of ionized-gas integrated spectra of COS-AGNi (Fig. A.4-A.8; see Sect. 4). For COS2949, we show the $H\alpha$ maps (Fig. A.9) since [O III] is outside of the wavelength range probed by JWST/NIRSpec IFU. For COS1638, we present the $H\alpha$ maps in the main text (see Fig. 3) given that the filament connecting the two AGNi is not visible in [O III]. Figures A.4-A.8 are complemented with the closeup of ionized-gas integrated spectra of the corresponding target between 4800-5060Å and 6460-6790Å (rest frame) showing the main rest-frame optical emission lines and their best fit models. Again, for COS2949 we only show the 6460-6790Å rest-frame range given that the JWST band starts at ≈ 5460 Å rest frame.

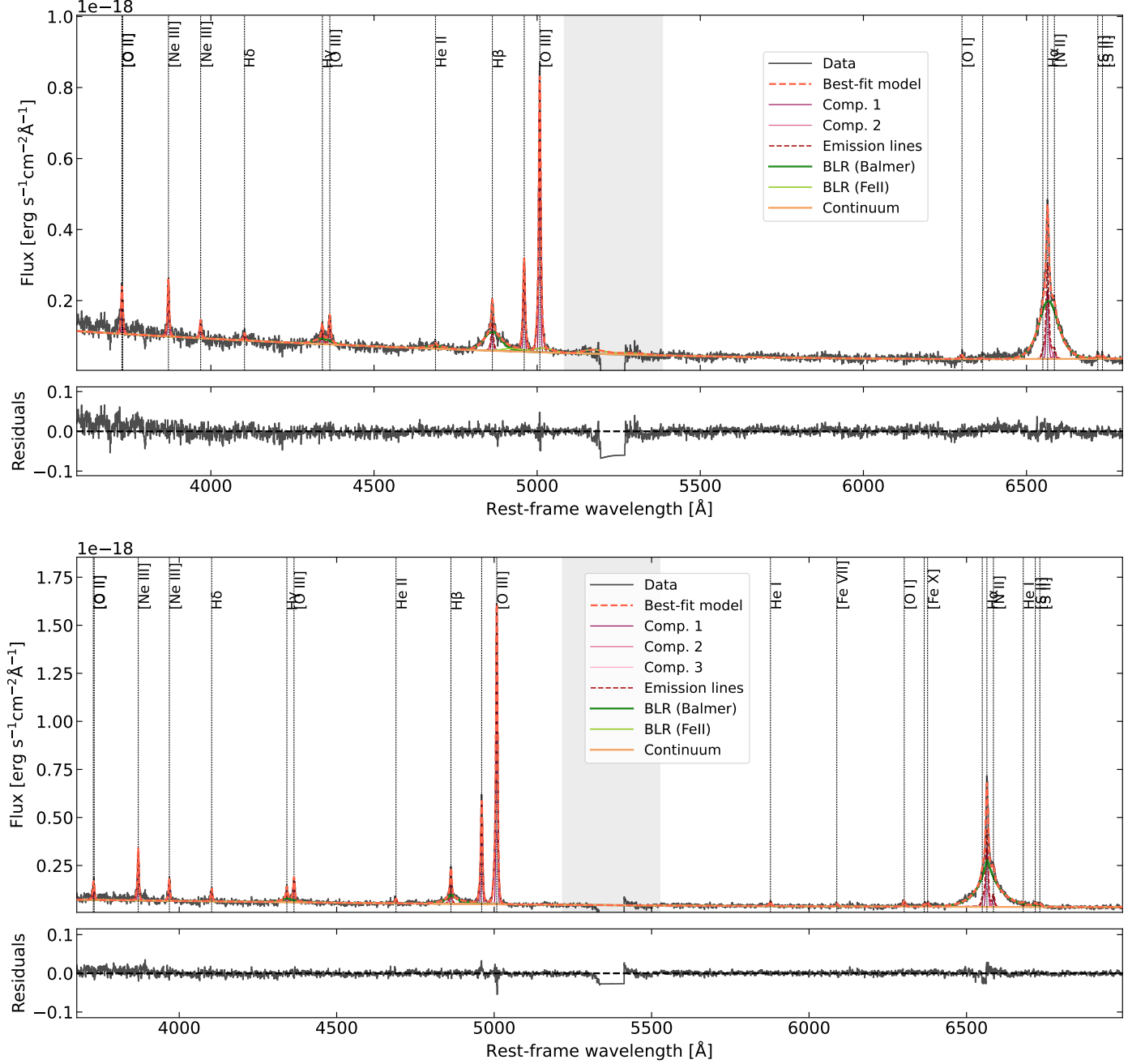


Fig. A.1: Nuclear spectra of COS1118 (Top) and COS590 (Bottom) used to produce the BLR template. Data and residuals are in black, total model is in dashed red, continuum is in orange, broad Balmer lines and FeII emission from the BLR are in dark and light green, respectively. FeII emission in these two targets is weak, and in COS590 almost marginal. Additional Gaussian emission line components are shown as dark to light purple and the total emission line model is shown as a dashed purple line. The gray shaded region marks the wavelength range that was excluded in the fitting process.

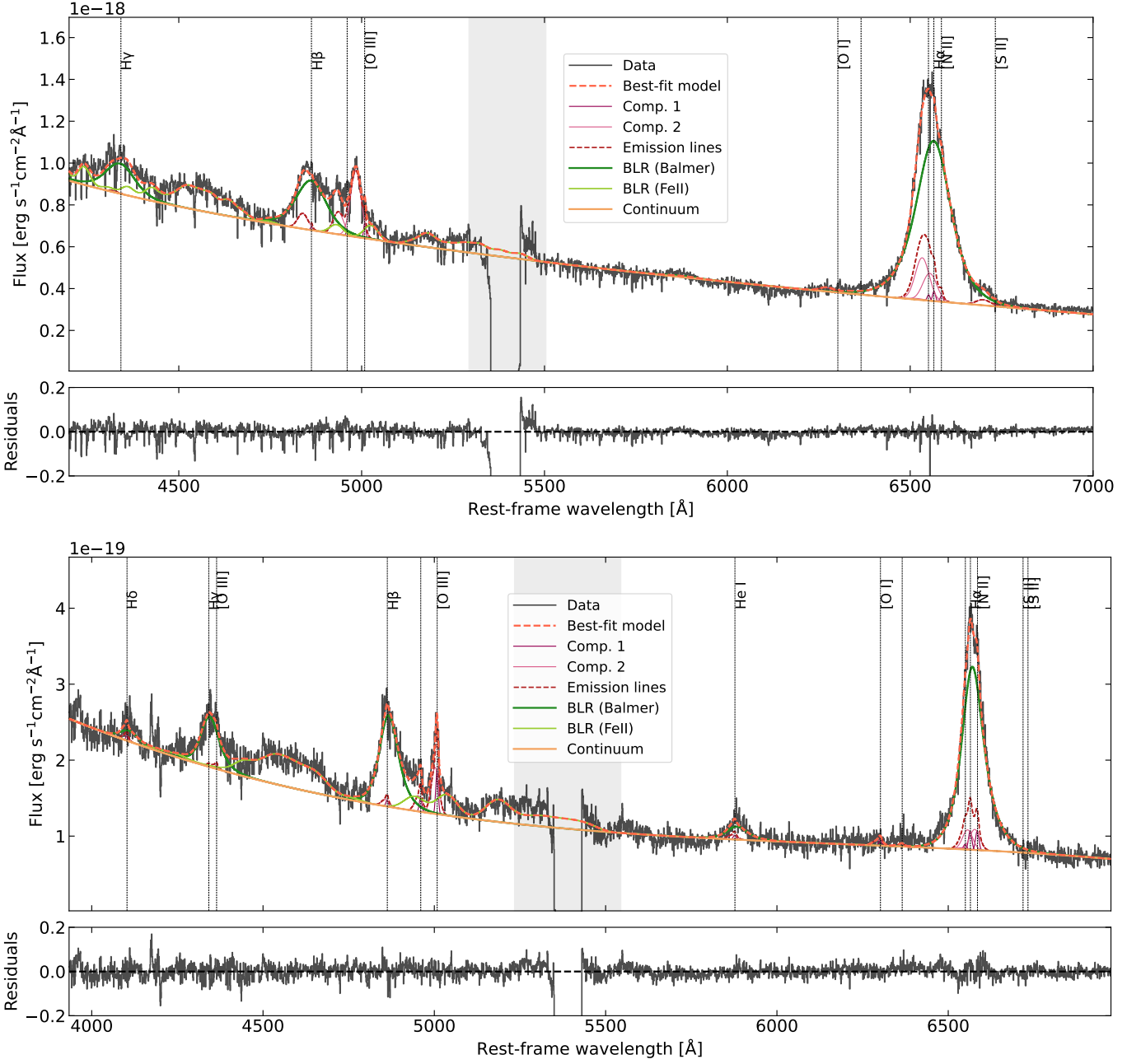


Fig. A.2: Nuclear spectra of COS1638-A (Top) and COS349 (Bottom) used to produce the BLR template. Color coding is as in Fig. A.1.

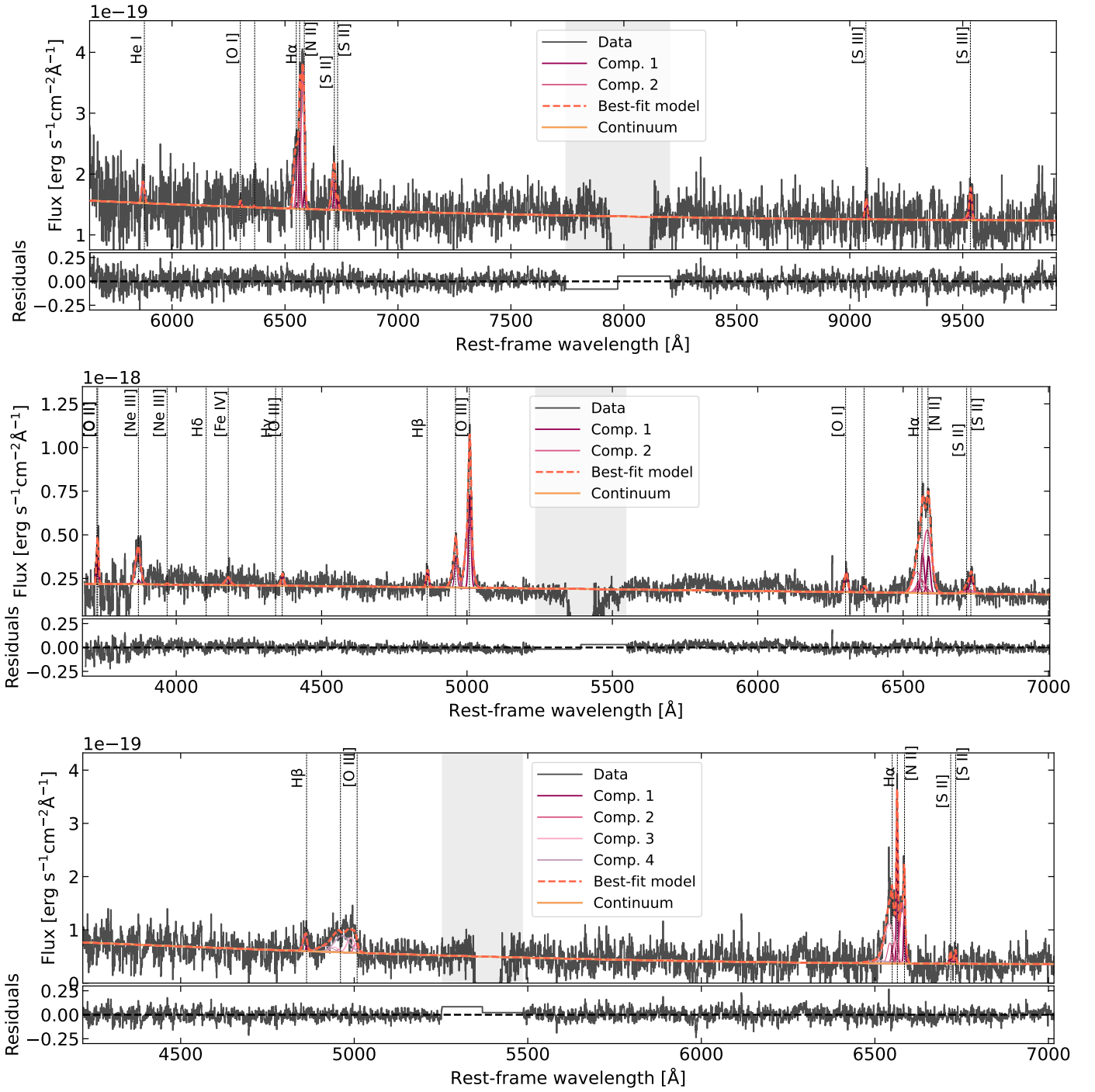


Fig. A.3: Spectra and best-fit models of COS2949 (Top), COS1656-A (Middle) and COS1638-B (Bottom) integrated over the outflow region ($S/N > 3$ mask of the broad emission). Data and residuals are in black, total model is in dashed red, continuum is in orange, additional Gaussian emission line components are shown as dark to light purple. The gray shaded region marks the wavelength range that was excluded in the fitting process.

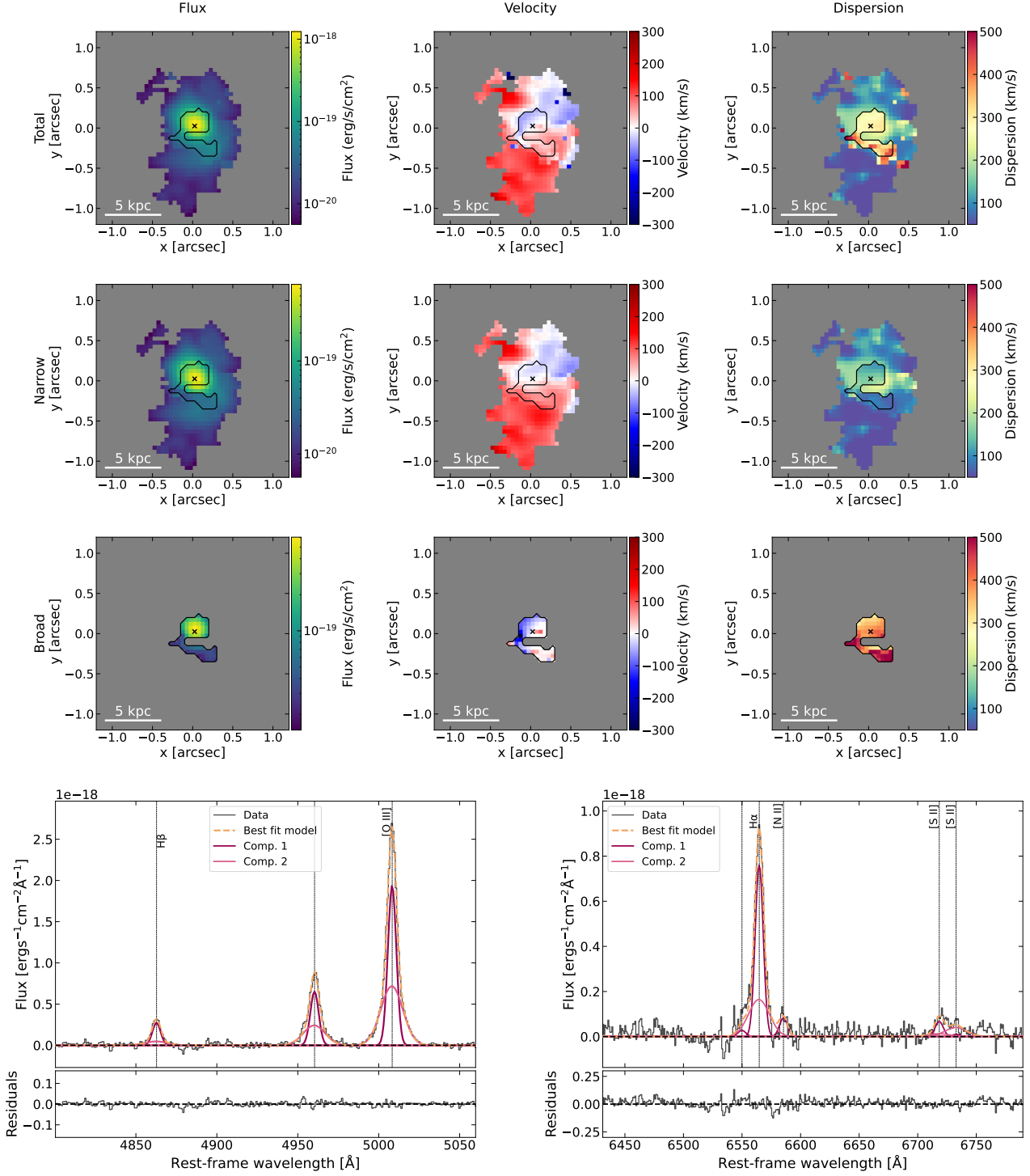


Fig. A.4: *Top*: [O III] maps of COS1118. From top to bottom: total, narrow and broad components. From Left to Right: flux, velocity and velocity dispersion. Black contours mark the outflow region used to produce the outflow-integrated spectra. *Bottom*: Close-up on the H β + [O III] complex (Left) and the H α + [N II] + [S II] complex (Right) of the continuum- and BLR-subtracted spectrum of COS1118 integrated over the 3σ mask of the broad [O III] emission. Data and residuals are in black, total model is in dashed orange, single line components are shown as dark to light purple. Component 1 corresponds to the narrow component, additional components add up to the broad component.

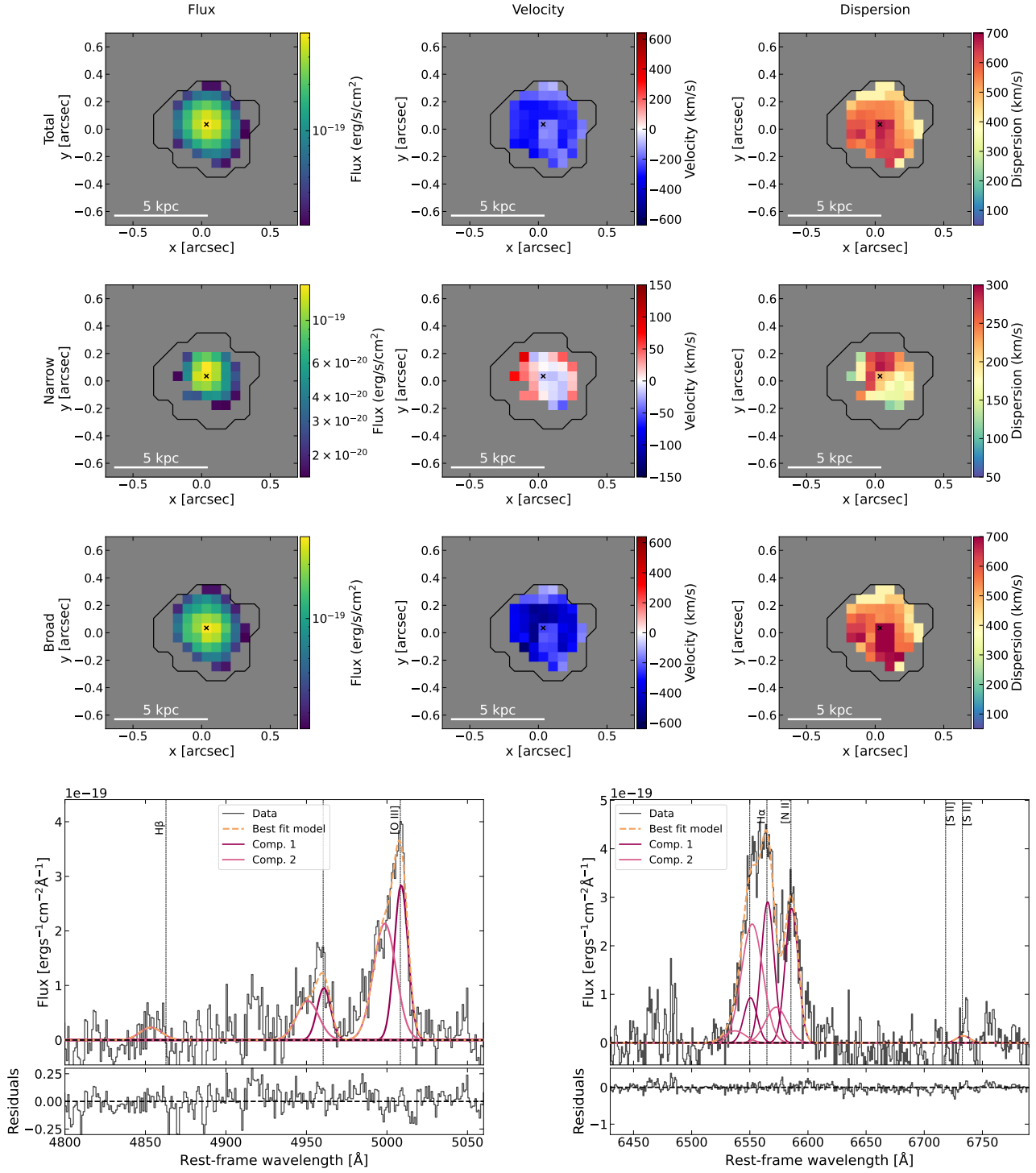


Fig. A.5: *Top*: [O III] maps of COS349. From top to bottom: total, narrow and broad components. From Left to Right: flux, velocity and velocity dispersion. Black contours mark the outflow region used to produce the outflow-integrated spectra. *Bottom*: Close-up on the H β + [O III] complex (Left) and the H α + [N II] + [S II] complex (Right) of the continuum- and BLR-subtracted spectrum of COS349 integrated over the 3σ mask of the broad [O III] emission. Data and residuals are in black, total model is in dashed orange, single line components are shown as dark to light purple. Component 1 corresponds to the narrow component, additional components add up to the broad component.

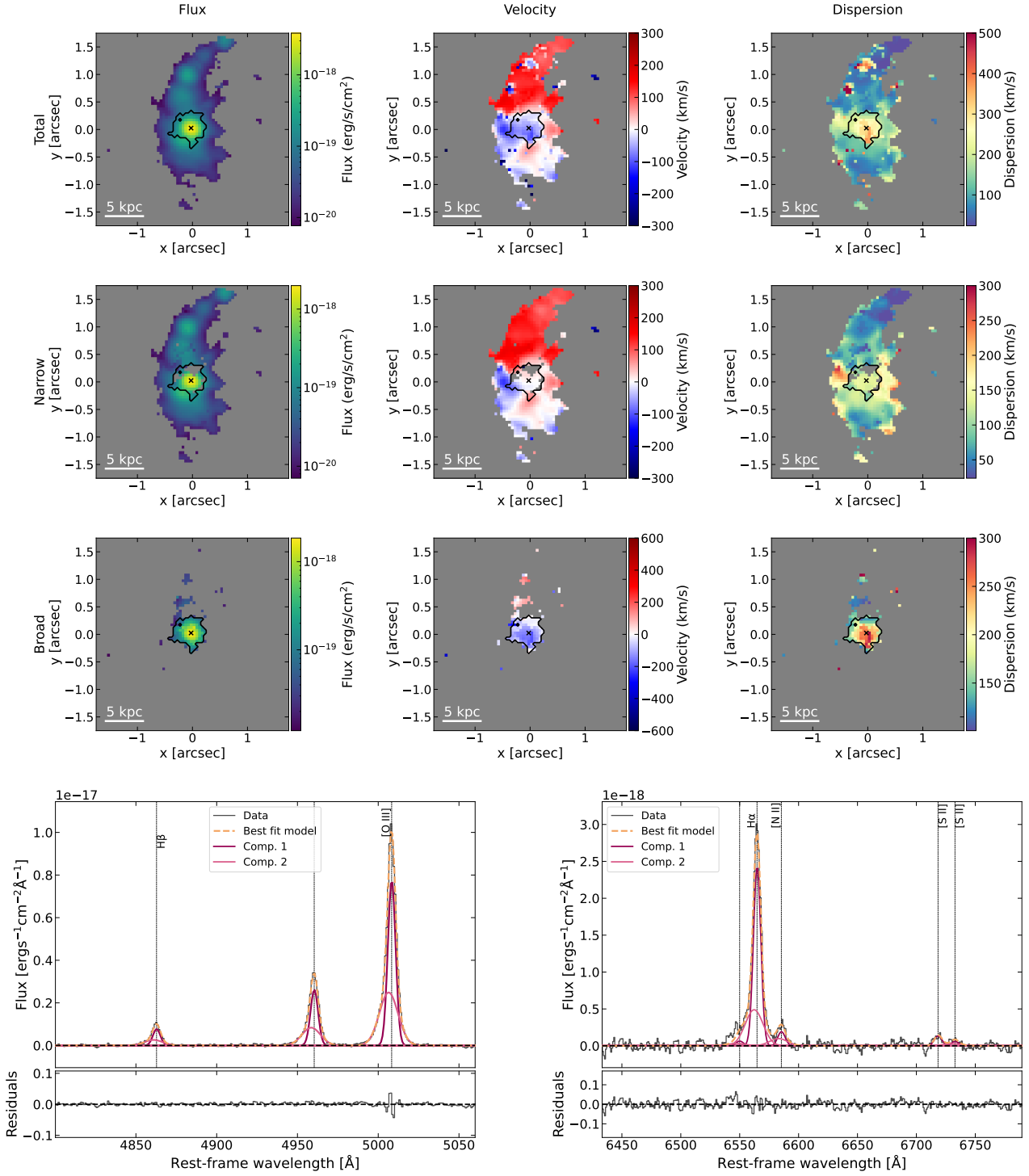


Fig. A.6: *Top*: [O III] maps of COS590. From top to bottom: total, narrow and broad components. From Left to Right: flux, velocity and velocity dispersion. Black contours mark the outflow region used to produce the outflow-integrated spectra. *Bottom*: Close-up on the H β + [O III] complex (Left) and the H α + [N II] + [S II] complex (Right) of the continuum- and BLR-subtracted spectrum of COS590 integrated over the 3σ mask of the broad [O III] emission, excluding the spaxels at the position of the other components northern of the AGN because possibly associated to tidal tails and not outflows. Data and residuals are in black, total model is in dashed orange, single line components are shown as dark to light purple. Component 1 corresponds to the narrow component, additional components add up to the broad component.

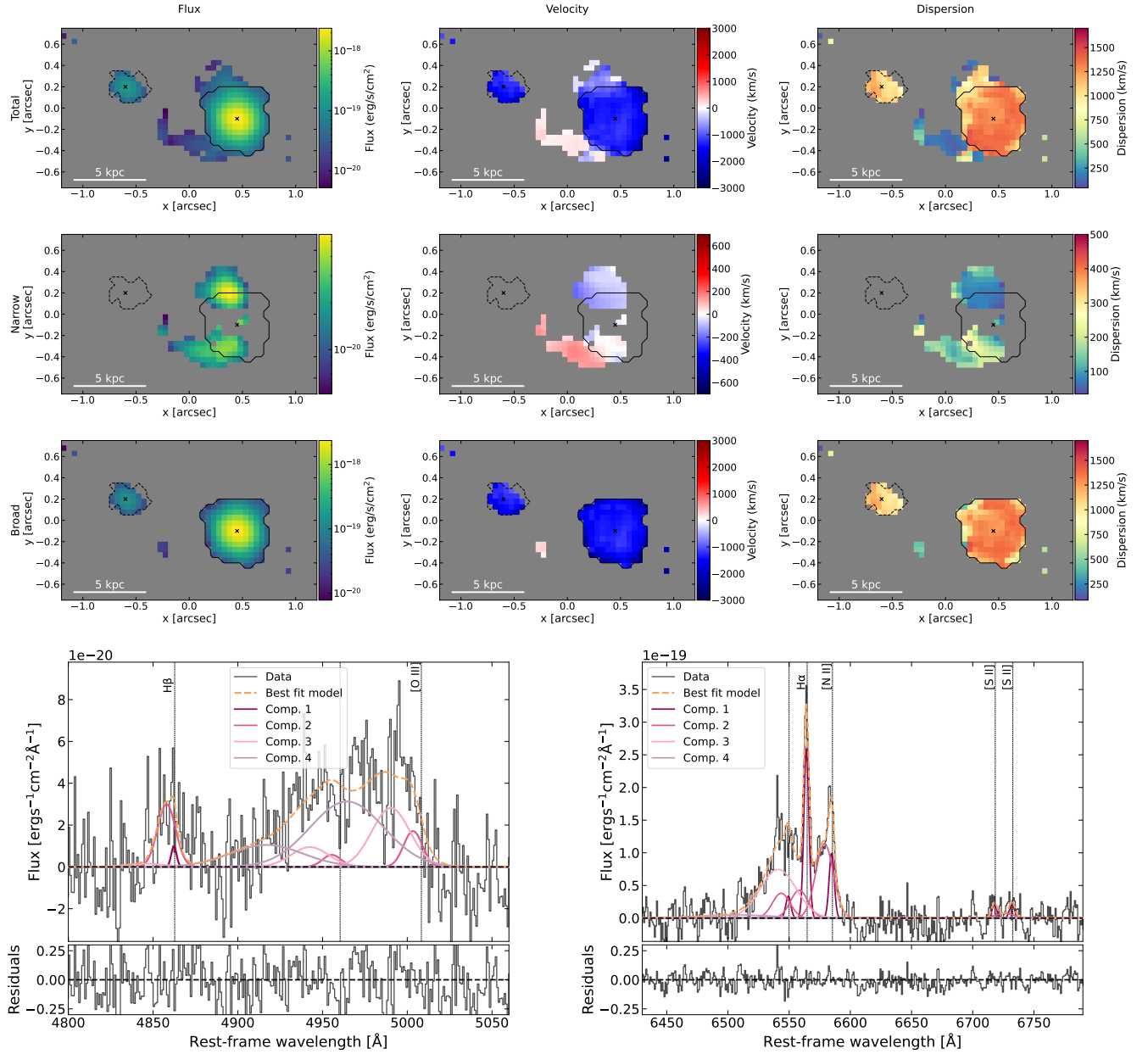


Fig. A.7: *Top*: $[\text{O III}]$ maps of COS1638 AGN A and B. From top to bottom: total, narrow and broad components. From Left to Right: flux, velocity and velocity dispersion. Solid (dashed) black contours mark the outflow region used to produce the outflow-integrated spectra of COS1638-A (COS1638-B). *Bottom*: Close-up on the $\text{H}\beta$ + $[\text{O III}]$ complex (Left) and the $\text{H}\alpha$ + $[\text{N II}]$ + $[\text{S II}]$ complex (Right) of the continuum- and BLR-subtracted spectrum of COS1638 AGN B integrated over the 3σ mask of the broad $[\text{O III}]$ emission at the position of AGN A. Data and residuals are in black, total model is in dashed orange, single line components are shown as dark to light purple. Component 1 corresponds to the narrow component, additional components add up to the broad component.

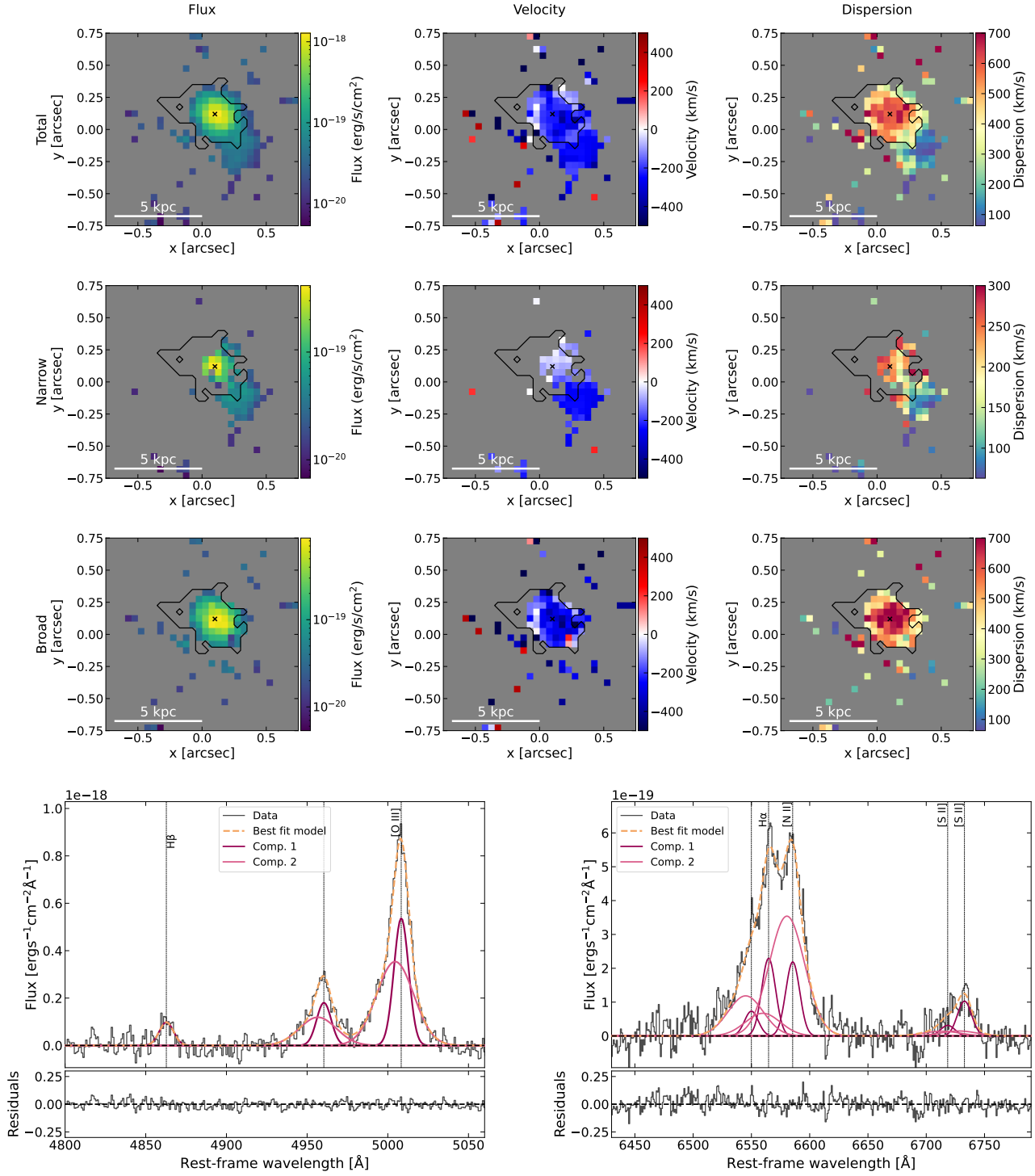


Fig. A.8: *Top*: [O III] maps of COS1656 AGN A. From top to bottom: total, narrow and broad components. From Left to Right: flux, velocity and velocity dispersion. Black contours mark the outflow region used to produce the outflow-integrated spectra. *Bottom*: Close-up on the H β + [O III] complex (Left) and the H α + [N II] + [S II] complex (Right) of the continuum- and BLR-subtracted spectrum of COS1656 AGN A integrated over the 3σ mask of the broad [O III] emission. Data and residuals are in black, total model is in dashed orange, single line components are shown as dark to light purple. Component 1 corresponds to the narrow component, additional components add up to the broad component.

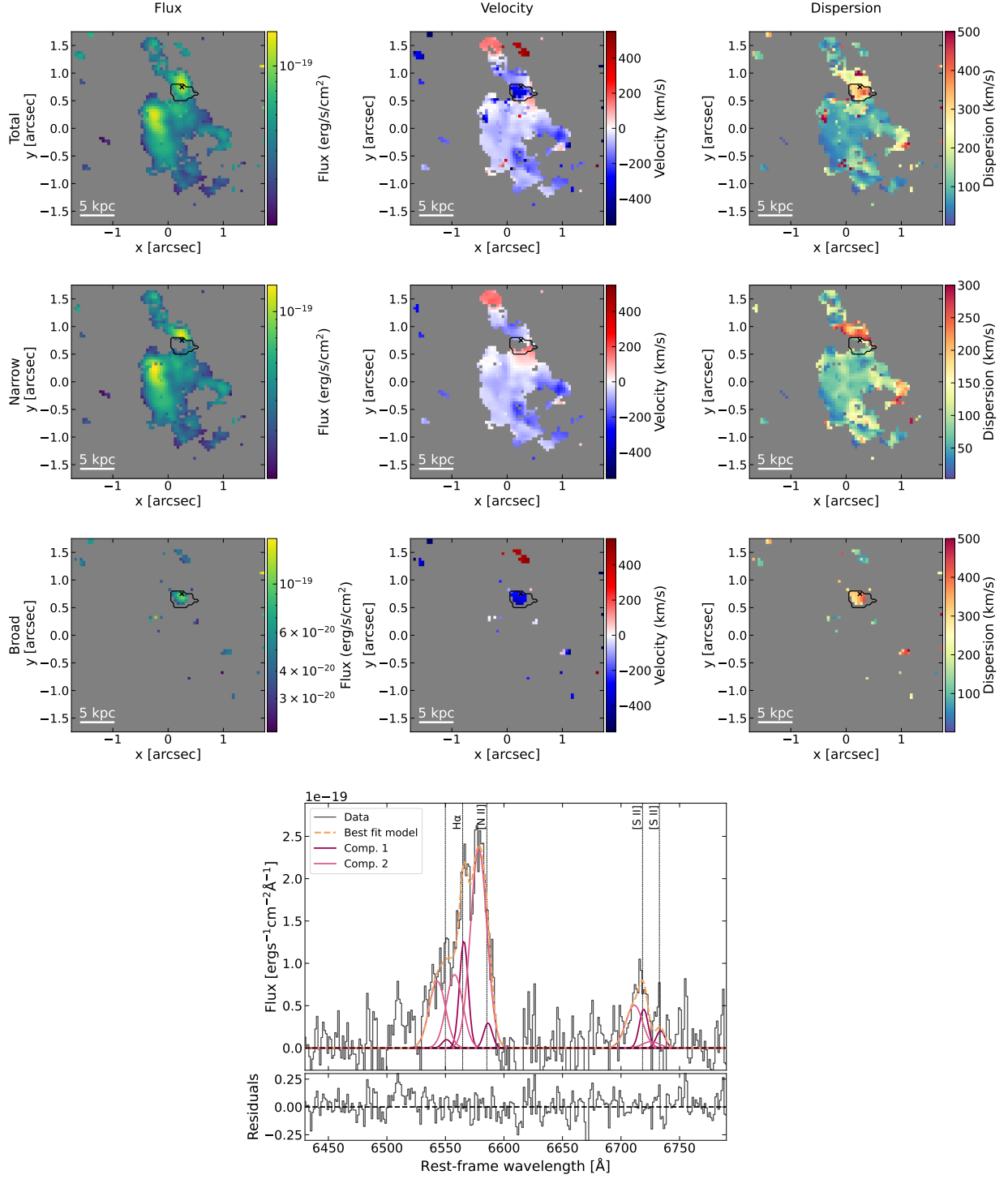


Fig. A.9: *Top*: $H\alpha$ maps of COS2949. From top to bottom: total, narrow and broad components. From Left to Right: flux, velocity and velocity dispersion. Black contours mark the flux levels of the corresponding kinematic component (total, broad, narrow) and they start at 3σ and increase by $5\times$. *Bottom*: Close-up on the $H\alpha$ + [N II] + [S II] complex (Right) of the continuum-subtracted spectrum of COS2949 integrated over the 3σ mask of the broad [N II] emission. Data and residuals are in black, total model is in dashed orange, single line components are shown as dark to light purple. Component 1 corresponds to the narrow component, additional components add up to the broad component.